

Chapter 2

Methods

2.1 Mathematical Background

An important class of results generated by biophysical research in the twentieth century is that of mathematical models, both of complete biological systems and of their constituting parts. A major breakthrough was the mathematical description of cell electrophysiology, beginning with the modeling of action potential propagation in the giant squid axon (a large nerve fiber) by Hodgkin and Huxley. In fact, their paper [1] is a summary of a series of preceding publications by Hodgkin et al. [2–5]. At the time, its novelty lay in the fact that the authors not only systematically studied transmembrane currents of different ion species using the newly established method of voltage clamp [6, 7]. They also gathered enough data on the voltage-determined, ion-specific permeability¹ of the membrane to combine all of their findings in a mathematical framework that accurately reproduces the experimental action potentials, including propagation along the nerve fiber.

Their results have essentially remained valid despite the progress that has been made in the discovery of molecular mechanisms leading to the observed ion current dynamics. This fact emphasizes the broad range of applicability of their method which is independent of the internal functioning of the biological substrate and thus rootedly empirical. D. Noble was one of the first to apply the model to cardiac excitable tissue, such as Purkinje fibers [8, 9]. All modern schemes of building electrophysiological models of excitable cells such as neurons, cardiomyocytes or muscle cells are still based on this method, merely using improved and more detailed experimental tools for identifying the active membrane proteins such as the patch clamp technique [10] and expression systems for ion channels [11]. Such models are therefore called Hodgkin-Huxley type models.

In the following sections, the necessary theoretical background for modeling cardiac tissue (and excitable media in general) will be introduced. They form the basis of

¹ The molecular basis of this variable permeability of the membrane (ion channels, cf. Sect. 1.2) was not known at the time.

all numerical work in this thesis. Following this fundamental theoretical framework, the specific models and analysis methods utilized in this work will be presented. In addition to the above-mentioned electrophysiology, a full mathematical description of cardiac tissue (up to the state of current knowledge) would have to cover many more aspects than just the pure electrophysiology, the most evident of them being excitation-contraction coupling—indispensable for the normal physiological function. However, using Occam’s razor, the presented methods will be restricted to those aspects that are necessary to understand the results in Sect. 2.3. It should also be noted that, despite the general agreement on the nature of action potentials in excitable cells and the huge system of theories that is based on the pioneering work by Hodgkin and Huxley, there is also a recent alternative explanation of propagating nerve impulses based on soliton waves in traveling in the cell membrane [12–14], which is, however, highly controversial and shall not be elaborated further upon in this work.

2.1.1 Single Cell Dynamics

Following Hodgkin’s and Huxleys’s scheme, the electrical behavior of the cell membrane can be modeled by an equivalent circuit as shown in Fig. 2.1: The (impermeable part of the) cell membrane is represented by a capacitor with capacity C_m . It can be charged by the accumulation of charge on its two plates (the inner and outer surfaces of the cell membrane) and the potential difference $V_m = v_i - v_e$ between the *intra-cellular* and the *extracellular potential* is called membrane potential, as explained in Sect. 1.2.1. This happens through passive and active ion channels that determine the permeability and thus the electrical conductivity of the membrane for specific ionic species (g_x for ion species x). Denoting the current through the membrane of ion species x by I_x and the charge on the capacitor by Q , Kirchhoff’s current law implies that the sum of all currents (through the vertical elements in Fig. 2.1) is zero

$$0 = \frac{dQ}{dt} + I_{\text{pump}} + I_{\text{Na}^+} + I_{\text{K}^+} + I_{\text{Ca}^{2+}} + I_{\text{Cl}^-} + I_{\dots} \quad (2.1)$$

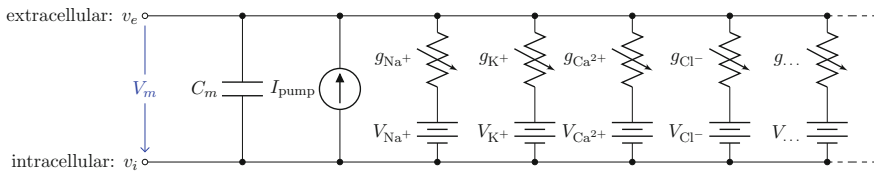


Fig. 2.1 Equivalent circuit diagram for the cell membrane. The cell membrane is modeled as a capacitor that is charged to the membrane voltage V_m by the Nernst potentials (V_{Na^+}, \dots) of different ion species. Variable resistors indicate varying individual permeability of the membrane for each ion species. The current source corresponds to ion transporters in the membrane necessary for ion homeostasis

$$\Rightarrow \frac{dQ}{dt} = C_m \frac{dV_m}{dt} = -I_{\text{pump}} - I_{\text{Na}^+} - I_{\text{K}^+} - I_{\text{Ca}^{2+}} - I_{\text{Cl}^-} - I_{\dots} \quad (2.2)$$

resulting in the above equation for the membrane potential V_m . In the above equation, the convention was used that positive currents point out of the cell, i.e. from intracellular to extracellular, which implies that the charge Q is the one on the intracellular “plate” of the capacitor. The right hand side is sometimes summarized in a term I_{ion} . Each term I_x , according to the circuit diagram in Fig. 2.1 is of the form

$$I_x = g_x(V_m - V_x), \quad (2.3)$$

where V_x is the reversal potential of the ion species x . The dots in Eq. (2.2) and Fig. 2.1 represent additional ion species and dynamic elements that could be included in the model. Due to the existence of multiple ion channel types for the same ionic species, the currents associated with each species in Fig. 2.1 have to be interpreted as net currents and g_x as a net (average) conductivity. Thus, the model could be refined by treating each ion channel type as a separate circuit element. This is indeed done in physiologically detailed models such as the Wang-Sobie model [15], but it is not necessary for the purpose of this thesis.

In contrast, an important aspect that has to be taken into account and that is at the basis of the nonlinear phenomenon of action potential formation is the variability of the conductances g_x . These are functions of time as well as the quantity gating the channel (membrane potential, individual ion concentrations or mechanical stress, cf. Sect. 1.2.1 and Ref. [16]). As mentioned in the introduction of this chapter, the development of the Hodgkin-Huxley formalism preceded the discovery of the molecular functioning of ion channels. Still, from the measured current traces in voltage clamp experiments, it was already clear that the dynamics of the individual ion conductances can themselves only be modeled by dynamical systems for the so-called *gating variables*. These describe the transitions between different states of the ion channel or its subunits, the main parameters being the transition rates that are, in turn, determined by the quantity responsible for gating the channel (e.g., V_m for voltage-gated channels). Depending on the absolute number of channels, a stochastic or deterministic model for the gating variables is required to accurately model the overall membrane conductance for a particular ionic species [17, 18]. As this thesis deals with macroscopic systems only, deterministic dynamics modeled by differential equations will be assumed in the following. In general, each current term in Eq. (2.2) is thus supplemented by a number of additional ordinary differential equations describing its (in-)activation dynamics. The full system of equations describing a single cell electrophysiological model in its most abstract form thus reads

$$\begin{aligned} C_m \frac{dV_m}{dt} &= \overbrace{-I_{\text{ion}}(V_m, \mathbf{h})}^{-I_{\text{pump}}(V_m, \mathbf{h}) - \sum_x I_x(V_m, \mathbf{h})} \\ \frac{d\mathbf{h}}{dt} &= \mathbf{H}(V_m, \mathbf{h}), \end{aligned} \quad (2.4)$$

where the vector \mathbf{h} consists of the gating and all further variables necessary to model the individual components (this may also include ion concentrations, etc.). All current electrophysiological cell models have the form of Eq. (2.4) and the number of terms on the right hand side varies with model complexity, either absorbing many summands into one term or splitting some of them up into individual contributions (see Sect. 2.1.6 for details).

2.1.2 Bi-domain Description of Cardiac Tissue

The single-cell model introduced in Sect. 2.1.1 can be thought of as a description for an average piece of the cell membrane without any spatial extent. In this case, C_m , Q and the current I_{ion} in Eq. (2.4) have to be interpreted as capacitance, charge and current *per unit membrane area*. This can be used to construct a model of a d -dimensional domain of cardiac tissue by extending the so-called *core conductor* model of neuronal *cable theory* [19], an idea that emerged during efforts in the 1970s to model surface electrocardiograms [20–22]. The resulting mathematical framework is currently viewed as the standard and most accurate model of cardiac tissue as a continuum [23–25]. If an extended slab of cardiac tissue is considered, the intracellular potentials, $v_i(\mathbf{x}, t)$ and $v_e(\mathbf{x}, t)$, respectively, become functions of the position \mathbf{x} in space, i.e. $\mathbf{x} \in \mathbb{R}^d$, $t \in \mathbb{R}$. The idea behind this is that both intracellular and extracellular spaces are defined in the whole tissue domain (thus occupying the same physical space) and have conductivity tensors $\underline{\sigma}_i$ and $\underline{\sigma}_e$, respectively, that are averaged quantities over multiple cells. The relative volumes of the physical intracellular and extracellular spaces and the geometrical arrangement of cells are implicitly contained in these averaged conductivities, as is the additional resistance introduced by gap junctions in the intracellular domain. The two domains represent spatially extended versions of the capacitor plates considered in the single cell model. Current densities *within* each domain caused by the corresponding potentials are:

$$\begin{aligned} \mathbf{j}_i &= -\underline{\sigma}_i \nabla v_i \\ \mathbf{j}_e &= -\underline{\sigma}_e \nabla v_e \end{aligned} \quad (2.5)$$

The current densities enter continuity equations for the charge densities q_i and q_e in the intracellular and extracellular domain, respectively. It is assumed that no charge accumulates anywhere in the tissue, such that $\partial q_i / \partial t = -\partial q_e / \partial t =: \partial q / \partial t$ and

$$\begin{aligned} \nabla \cdot \mathbf{j}_i + \frac{\partial q}{\partial t} &= -i_{\text{ion}} \\ \nabla \cdot \mathbf{j}_e - \frac{\partial q}{\partial t} &= i_{\text{ion}}, \end{aligned} \quad (2.6)$$

where the lowercase quantities q and i_{ion} are charge and membrane current *per unit volume*, respectively. Otherwise, the same sign conventions as in Sect. 2.1.1

apply. The membrane currents appear as sources and sinks for the extracellular and intracellular domain, respectively, as crossing the cell membrane is the only way for charge to leave one of the two domains (in the absence of current injection via electrodes). As the corresponding quantities Q and I_{ion} are given per unit membrane area, these quantities have to be converted using the surface-to-volume ratio β (units: area per volume) which specifies how much membrane surface there is on average for a given volume of tissue. Combining Eqs. (2.5) and (2.6), the *Bi-domain equations* for the tissue domain \mathcal{D} are obtained:

$$\nabla \cdot \underline{\sigma}_i \nabla v_i = -\nabla \cdot \mathbf{j}_i = \beta \left(\frac{\partial Q}{\partial t} + I_{\text{ion}} \right) = \beta \left(C_m \frac{\partial(v_i - v_e)}{\partial t} + I_{\text{ion}} \right) \quad \text{in } \mathcal{D} \quad (2.7a)$$

$$\nabla \cdot \underline{\sigma}_e \nabla v_e = -\nabla \cdot \mathbf{j}_e = -\beta \left(\frac{\partial Q}{\partial t} + I_{\text{ion}} \right) = -\beta \left(C_m \frac{\partial(v_i - v_e)}{\partial t} + I_{\text{ion}} \right) \quad \text{in } \mathcal{D} \quad (2.7b)$$

These equations have to be completed by boundary conditions for v_i and v_e at the boundary $\partial\mathcal{D}$ of the tissue domain \mathcal{D} . Assuming the space outside the tissue domain \mathcal{D} is a mono-domain with conductivity $\underline{\sigma}_o$ and a corresponding *outside potential* v_o , these boundary conditions are

$$\mathbf{n} \cdot \underline{\sigma}_i \nabla v_i = 0 \quad \text{on } \partial\mathcal{D} \quad (2.8a)$$

$$v_e = v_o \quad \text{on } \partial\mathcal{D} \quad (2.8b)$$

$$\mathbf{n} \cdot \underline{\sigma}_e \nabla v_e = \mathbf{n} \cdot \underline{\sigma}_o \nabla v_o \quad \text{on } \partial\mathcal{D} \quad (2.8c)$$

where \mathbf{n} is a local unit vector perpendicular to the boundary $\partial\mathcal{D}$. Equation (2.8a) is a no-flux boundary condition, expressing the fact that the intracellular space ends at the tissue boundary and thus no current *in* the intracellular domain can cross this boundary. Equations (2.8b) and (2.8c) ensure the continuity of the extracellular potential and currents at the interface between the extracellular space inside the tissue and the mono-domain outside the tissue (e.g., the bath).

For practical calculations, a different linear combination of the system (2.7) is used which corresponds to a change of variables from v_i and v_e to $V_m = v_i - v_e$ and v_e :

$$\begin{aligned} \nabla \cdot \underline{\sigma}_i \nabla \overbrace{(V_m + v_e)}^{v_i} &= \beta \left(C_m \frac{\partial V_m}{\partial t} + I_{\text{ion}} \right) \quad \text{in } \mathcal{D} \\ \nabla \cdot \underline{\sigma}_e \nabla v_e &\stackrel{(2.7a+2.7b)}{=} -\nabla \cdot \underline{\sigma}_i \nabla v_i = -\nabla \cdot \underline{\sigma}_i \nabla (V_m + v_e) \quad \text{in } \mathcal{D} \end{aligned}$$

Reordering the terms in both equations yields

$$C_m \frac{\partial V_m}{\partial t} = \frac{1}{\beta} \nabla \cdot \underline{\sigma}_i \nabla (V_m + v_e) - I_{\text{ion}}(V_m, \mathbf{h}) \quad \text{in } \mathcal{D} \quad (2.9a)$$

$$\frac{\partial \mathbf{h}}{\partial t} = \mathbf{H}(V_m, \mathbf{h}) \quad \text{in } \mathcal{D} \quad (2.9b)$$

$$\nabla \cdot (\underline{\sigma}_e + \underline{\sigma}_i) \nabla v_e = -\nabla \cdot \underline{\sigma}_i \nabla V_m \quad \text{in } \mathcal{D}. \quad (2.9c)$$

Having been omitted so far, Eq. (2.9b) was reinserted from Eq. (2.4) for completeness. Equation (2.9c) does not contain t and thus states that the extracellular potential can be determined from the membrane potential at any given instant. In Eq. (2.9a), the term $\nabla \cdot \underline{\sigma}_i \nabla (V_m + v_e)$ is more favorable than the seemingly simpler $-\nabla \cdot \underline{\sigma}_e \nabla v_e$, because in this way, the equation stays valid in the limit $\underline{\sigma}_e = \alpha \underline{\sigma}_e^*$ for $\alpha \rightarrow \infty$. This will be useful in the next section. For the boundary conditions (2.8), the change of variables can be achieved by replacing V_m in Eq. (2.8a):

$$\mathbf{n} \cdot \underline{\sigma}_i \nabla (V_m + v_e) = 0 \quad \text{on } \partial \mathcal{D} \quad (2.10a)$$

$$v_e = v_o \quad \text{on } \partial \mathcal{D} \quad (2.10b)$$

$$\mathbf{n} \cdot \underline{\sigma}_e \nabla v_e = \mathbf{n} \cdot \underline{\sigma}_o \nabla v_o \quad \text{on } \partial \mathcal{D} \quad (2.10c)$$

2.1.3 Mono-domain Descriptions of Cardiac Tissue

For full numerical simulations using the bi-domain equations (2.9), one would have to time-step the membrane potential V_m using Eq. (2.9a) from a given present state and calculate the corresponding extracellular potential by solving Eq. (2.9c) for v_e . The latter requires solving a large system of linear equations, an operation that is computationally very costly. Because of this, there exists an approximation that only involves a single *partial differential equation* (PDE) for V_m that can be solved by time stepping, the so-called *mono-domain equation*. Although the mono-domain model is used extensively in the literature and is regarded a valid model in its own right without further justification, it is important to know its connection to the full and more realistic bi-domain formulation. In particular, this is true for understanding the effects of electric fields near tissue boundaries, which is one of the aims of this thesis. In the following two sub-sections, two different ways of deriving the mono-domain equation with different physical interpretation will be presented. When working with a mono-domain equation, one has to ensure that modifications to the equations are consistent with the choice of interpretation.

2.1.3.1 Neglecting the Extracellular Potential

Assume a very well-conducting extracellular space,² i.e. $\alpha \gg 1$ for $\underline{\sigma}_e = \alpha \underline{\sigma}_e^*$. In the limit $\alpha \rightarrow \infty$, Eq. (2.9c) reduces to $\nabla \cdot \underline{\sigma}_e^* \nabla v_e = 0$. This means that for large α the source term for the extracellular potential becomes negligible and one possible form of solution is $v_e = -\mathbf{E} \cdot \mathbf{x} + c$ with some fixed electric field vector \mathbf{E} and an arbitrary constant c (if boundary conditions (2.10b) and (2.10c) permit).³ For this solution, it has to be assumed that $\underline{\sigma}_e^*$ is spatially constant. If we assume the extracellular space is insulated ($\mathbf{n} \cdot \underline{\sigma}_e^* \nabla v_e = 0$) or grounded ($v_e = 0$) on $\partial\mathcal{D}$, this solution reduces even further to $v_e = c$ or $v_e \equiv 0$, respectively. In contrast, Eq. (2.9a) is still valid. The mono-domain equation in this scenario therefore is

$$\frac{\partial V_m}{\partial t} = \nabla \cdot \underline{D} \nabla (V_m + v_e) - I_{\text{ion}}/C_m \quad \text{in } \mathcal{D}, \quad (2.11)$$

where the diffusion tensor is given by $\underline{D} = \underline{\sigma}_i/(\beta C_m)$ and v_e is merely a parameter for the problem, which is usually set to zero following the line of thoughts above. To make this problem well-defined, the boundary condition (2.10a) is sufficient:

$$\mathbf{n} \cdot \underline{D} \nabla (V_m + v_e) = 0 \quad \text{on } \partial\mathcal{D} \quad (2.12)$$

2.1.3.2 Equivalent Mono-domain Description

In Sect. 2.1.3.1, a mono-domain formulation of the bi-domain model was obtained by changing the physics of the problem. The extent to which the dynamics is altered can be significantly reduced in the case where the intracellular and extracellular conductivity tensors are scaled versions of the same tensor: $\underline{\sigma}_e = \alpha \underline{\sigma}_i$. In this case, Eq. (2.7b) can be subtracted from Eq. (2.7a):

$$\nabla \cdot \underline{\sigma}_i \nabla V_m = \left(1 + \alpha^{-1}\right) \beta \left(C_m \frac{\partial V_m}{\partial t} + I_{\text{ion}} \right)$$

Rearranging for $\partial V_m / \partial t$ yields the mono-domain equation

$$\frac{\partial V_m}{\partial t} = \nabla \cdot \underline{D} \nabla V_m - I_{\text{ion}}(V_m, \mathbf{h})/C_m \quad \text{in } \mathcal{D} \quad (2.13a)$$

$$\frac{\partial \mathbf{h}}{\partial t} = \mathbf{H}(V_m, \mathbf{h}) \quad \text{in } \mathcal{D} \quad (2.13b)$$

² Incidentally, this case brings the model of cardiac tissue very close to the neuronal cable equation from which it branched off. There, the assumption of an infinite conductivity in the extracellular space is justified by the large amount of fluid that surrounds the axon.

³ Other solutions are possible, viz. all those for which a vector potential \mathbf{A} exists with $\underline{\sigma}_e^* \nabla v_e = \nabla \times \mathbf{A}$. For $v_e = -\mathbf{E} \cdot \mathbf{x}$, choose $\mathbf{A} = -((\underline{\sigma}_i \mathbf{E})_{3x_2}, (\underline{\sigma}_i \mathbf{E})_{1x_3}, (\underline{\sigma}_i \mathbf{E})_{2x_1})^T$.

where now $\underline{D} = \underline{\sigma}_i / [\beta C_m (1 + \alpha^{-1})]$. In the limit $\alpha \rightarrow \infty$, the definition of \underline{D} is equal to that in Eq. (2.11). Similarly, the v_e term in Eq. (2.11) becomes irrelevant if $\underline{\sigma}_e^*$ is a scaled $\underline{\sigma}_i$, because then $\nabla \cdot \underline{D} \nabla v_e = 0$ follows from $\nabla \cdot \underline{\sigma}_e^* \nabla v_e = 0$. Equations (2.11) and (2.13) are thus consistent in the sense that they are equivalent when the assumptions for both mono-domain descriptions are fulfilled.

Note that the mono-domain description (2.13) is completely equivalent to the full bi-domain model, but numerically cheap compared to Eq. (2.9). Consequently, for the case $\underline{\sigma}_e = \alpha \underline{\sigma}_i$, numerical simulation of the bi-domain model is usually superfluous. There is, however, one caveat: from the set of boundary conditions (2.10), no boundary condition for the membrane potential alone can be derived. Also, unlike in Eq. (2.11), v_e is not decoupled from the membrane potential dynamics and so Eq. (2.10a) cannot be enforced unless v_e is calculated, which would defeat the original purpose of a mono-domain formulation. The usual (somewhat nonphysical) solution to this dilemma is to apply the ad-hoc *no-flux boundary condition*

$$\mathbf{n} \cdot \underline{D} \nabla V_m = 0 \quad \text{on } \partial \mathcal{D}. \quad (2.14)$$

This is sufficient for modeling the dynamics inside a tissue domain \mathcal{D} , where the boundary of the domain is not meant to be a physical part of the system but rather a computational necessity. However, it is only a valid simplification, if one can rule out any influence of the boundary condition on the effects one wants to study. Sometimes, the no-flux boundary condition is physically justified, for example, if the extracellular space is known to be insulated electrically at the tissue boundary. However, in particular in this thesis, investigating effects at the boundaries of the tissue due to the conductive connection of the extracellular space to the surrounding environment is the original purpose of the modeling. In this case, an alternative solution is to assume that α and the outside conductivity $\underline{\sigma}_o$ are large, which decouples the corresponding potentials from the dynamics of the membrane potential and makes them parameters as seen for Eq. (2.11). This way, an extracellular or outside potential (e.g., a uniform electric field) can be assumed rather than calculated, which makes it possible to use Eq. (2.10a) itself or a boundary condition obtained by subtracting Eq. (2.10c) from Eq. (2.10a):

$$\mathbf{n} \cdot \underline{D} \nabla (V_m + v_e) = 0 \quad \text{on } \partial \mathcal{D} \quad (2.15)$$

or

$$\mathbf{n} \cdot \underbrace{\alpha \underline{\sigma}_i}_{=\underline{\sigma}_e} \nabla V_m = -\mathbf{n} \cdot \underline{\sigma}_o \nabla v_o \quad \text{on } \partial \mathcal{D} \quad (2.16)$$

The second boundary condition (2.16) will be used in Sect. 3.2 to study the effect of electric fields near boundaries of the tissue. As for the bi-domain model (2.9), the mono-domain equation (2.13) has to be supplemented by a concrete model \mathbf{H} for the local variables \mathbf{h} and the corresponding ionic currents $I_{\text{ion}}(V_m, \mathbf{h})$. The models used in this thesis will be introduced in Sect. 2.1.6.

2.1.4 Anisotropy

Although all simulations in this thesis are carried out assuming isotropic diffusion, for completeness of the mathematical framework, the construction of the corresponding tensors for the specific requirements of cardiac tissue shall be mentioned here briefly: The anisotropic conductivity of cardiac tissue due to the fiber orientation and sheet structure of the muscle (see Sect. 1.3) can be implemented in the bi-domain and in the mono-domain model by choosing the diffusion tensor \underline{D} or equivalently the conductivity tensors. \underline{D} can be constructed from its three eigenvectors, each of which represents a direction in which a potential gradient leads to a current density in the same direction, with a conductivity equal to the corresponding eigenvalue. The fiber orientation determines one of these directions, the other two are uniquely defined by the normal vector of the laminar sheets (the remaining vector thus corresponds to the direction perpendicular to the fibers within the sheet). These three eigenvectors form an orthonormal basis of \mathbb{R}^3 , implying that \underline{D} must be a real, symmetric matrix. Using these properties, the entire tensor \underline{D} is determined by two unit vectors in space defining the fiber direction $\mathbf{f} = (f_x, f_y, f_z)$ and the direction normal to the sheet plane $\mathbf{n} = (n_x, n_y, n_z)$ and by diffusion constants D_{\parallel} along the fibers, D_{\perp} perpendicular to the fibers (within the sheet) and $D_{\perp\perp}$ normal to the sheets (see Eq. 17 in [25]):

$$D_{ij} = \delta_{ij}D_{\perp} + (D_{\parallel} - D_{\perp})f_i f_j + (D_{\perp\perp} - D_{\perp})n_i n_j, \quad i, j \in \{x, y, z\} \quad (2.17)$$

A common simplification is to ignore the sheet structure and thus assume $D_{\perp\perp} = D_{\perp}$, which eliminates one of the terms in Eq. (2.17). Note also that, in general, both the directions and diffusion constants may vary spatially.

The so-called *anisotropy ratio* is defined as the quotient D_{\parallel}/D_{\perp} . In the bi-domain equations, the two conductivity tensors $\underline{\sigma}_e$ and $\underline{\sigma}_i$ can be chosen independently. While the fiber orientation for both is the same, because it is given by the geometrical arrangement of the cells, the anisotropy ratio can be different. The case of equal anisotropy ratio is the one considered in the mono-domain approximation of Sect. 2.1.3.2.

2.1.5 The Phase-Field Method

As outlined in Sect. 2.1.3, boundary conditions constitute an important part of any problem described by a PDE on a spatial domain \mathcal{D} . It was mentioned that a widely-used boundary condition for mono-domain cardiac models is no-flux. Another possibility which was derived for the case of a predetermined extracellular/outside potential is that of Eq. (2.16) in the same section. Both boundary conditions are of the *Neumann* type, i.e. they fix the normal fluxes $\mathbf{n} \cdot \underline{D} \nabla u$ on the boundary $\partial\mathcal{D}$. As will be shown in Sect. 2.2.3, for a finite-difference numerical scheme, no-flux boundary conditions are straightforward to implement, if the boundaries of the

domain \mathcal{D} are parallel to the coordinate axes, e.g., rectangles in cartesian coordinates or (fractional) annuli in polar coordinates. For arbitrarily shaped domains \mathcal{D} , there is no such natural way of imposing zero flux on the domain boundary. In this case, one usually resorts to more complex and computationally intensive numerical schemes like *finite-volume* or *finite-element methods* (see Sect. 6.3 of Ref. [25] and references therein).

In Ref. [26], Fenton et al. introduce a phase-field method to impose no-flux boundary conditions on arbitrary geometries using finite differences on a simple (e.g., rectangular) computational domain \mathcal{D}_c which contains the actual physical domain \mathcal{D} . In the following, this method will be explained in detail and extended to arbitrary Neumann boundary conditions of the type of Eq. (2.16). Furthermore, mathematical improvements to the convergence proof will enable a better assessment of the method's numerical accuracy. The generalized method will be used extensively in Sect. 3.2 to study the effect of electric fields at boundaries of curved tissue domains.

2.1.5.1 Description of the Method

The phase-field method is based on defining a phase field ϕ , which is a smoothed version of the characteristic function of \mathcal{D} , i.e. $\phi \approx 1$ inside the domain $\mathcal{D} \subset \mathcal{D}_c$ and $\phi \approx 0$ otherwise, with a smooth transition in between. In this thesis, a different dynamical system than suggested in Ref. [26] shall be used for obtaining ϕ from the sharp, original characteristic function ϕ_0 :

$$\frac{\partial \phi}{\partial t} = (\phi_0 - \phi) + \xi^2 \Delta \phi. \quad (2.18)$$

In this equation, ϕ approaches a smooth phase field for $t \rightarrow \infty$, which stays close to ϕ_0 and has a diffusive boundary with a characteristic length scale ξ of the resulting transition at the interface between $\phi = 1$ and $\phi = 0$. It does not suffer from the stability issues in higher dimensions mentioned in [26] for the double-well potential method defined therein. Hence, any method that finds the equilibrium of Eq. (2.18) may be used instead of explicit time-stepping. In the following, this steady-state solution will be referred to as ϕ . An example for ϕ_0 and the resulting ϕ is depicted in Fig. 2.2a, b respectively. One property that will prove to be important for the line of thoughts below is that the normal slope of $\ln \phi$ decreases rapidly and monotonically within the interface region (in the outward direction) until reaching an approximately constant value on the order of $-1/\xi$, as shown in Fig. 2.2c. Hence, at large normal distances from the interface, ϕ decays approximately exponentially and $\partial^2 \ln \phi / \partial n^2 \approx 0$. As illustrated in Fig. 2.2d, the normal direction is defined by the direction of the gradient $\nabla \ln \phi$ itself.

The phase field method then consists of substituting the original diffusion term (e.g., in Eq. (2.13)) by a modified term that involves the phase field ϕ :

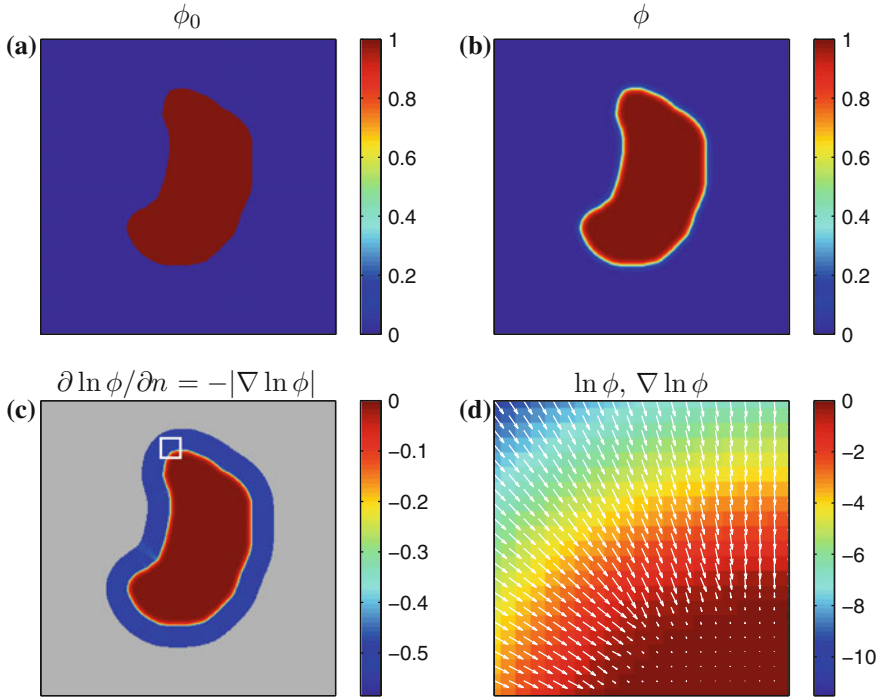


Fig. 2.2 Phase field behavior. **a** Initial binary phase field ϕ_0 , i.e. the characteristic function of \mathcal{D} . **b** Steady-state solution of Eq.(2.18) with ϕ_0 from (a) and $\xi = 2$. **c** $|\nabla \ln \phi|$ which is equal to $-\partial \ln \phi / \partial n$ if one defines the normal vector \mathbf{n} to be anti-parallel to $\nabla \ln \phi$. The logarithmic normal derivative increases quickly from 0 inside \mathcal{D} to an approximately constant value $\approx 1/\xi$ outside \mathcal{D} . **d** $\ln \phi$ shown as a *color plot* and the corresponding gradient shown as *arrows* for the region indicated by a *white rectangle* in (c)

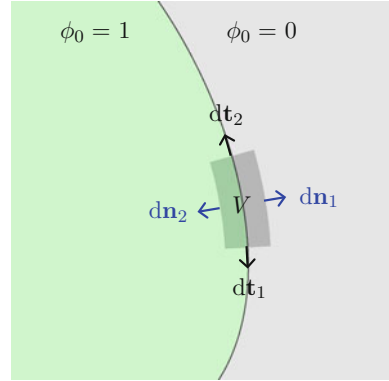
$$\nabla \cdot (\underline{D} \nabla u) \rightarrow \frac{1}{\phi} \nabla \cdot (\phi \underline{D} \nabla u) \quad (2.19)$$

The resulting PDE after the substitution is assumed to be defined on the whole domain \mathcal{D}_c , but only the part of the solution in $\mathcal{D} \subset \mathcal{D}_c$ is taken to have physical meaning. Fenton et al. present a mathematical argument in Ref. [26] for a one-dimensional tissue domain which suggests that the substitution (2.19) for \mathcal{D}_c leads to a solution in \mathcal{D} that obeys a no-flux boundary condition

$$\mathbf{n} \cdot (\underline{D} \nabla u) = 0 \quad \text{on } \partial \mathcal{D}. \quad (2.20)$$

A similar proof for higher dimensions based on the same idea was provided in Ref. [27]. In the following, this idea and its shortcomings in terms of the necessary mathematical assumptions will be presented and an argument will be given how these deficits may be resolved.

Fig. 2.3 Volume integration at the phase-field interface. Sketch of the integration volume for Eq. (2.22) parallel to the boundary $\partial\mathcal{D}$ which is defined by the border between $\phi_0 = 1$ (green) and $\phi_0 = 0$ (gray). Arrows indicate normal vectors on the surfaces of the integration volume corresponding to the individual terms in Eq. (2.23)



2.1.5.2 Original Convergence Proof

Omitting any additional non-spatial degrees of freedom for the reaction term, the general PDE for a reaction-diffusion system with the replacement of Eq. (2.19) is

$$\frac{\partial u}{\partial t} = f(u) + \frac{1}{\phi} \nabla \cdot (\phi \underline{D} \nabla u), \quad (2.21)$$

where f is assumed to be bounded for bounded u . The multi-dimensional equivalent of the mathematical argument given in [26] starts by integrating Eq. (2.21) over a small volume V across the boundary $\partial\mathcal{D}$, which yields

$$\int_V \phi \frac{\partial u}{\partial t} dV = \int_V \phi f(u) dV + \int_V \nabla \cdot (\phi \underline{D} \nabla u) dV = \int_V \phi f(u) dV + \oint_{\partial V} \phi \underline{D} \nabla u \cdot d\mathbf{A}. \quad (2.22)$$

The geometrical situation is illustrated in Fig. 2.3, with the volume V shaded gray. A similar strategy for a different integration path is given in Ref. [28], but the following argumentation applies universally. Denoting the individual contributions to the surface integral separately leads to

$$\begin{aligned}
\int_V \phi \frac{\partial u}{\partial t} dV &= \int_V \phi f(u) dV \\
&+ \int_{\partial V_n^1} \phi \underline{D} \nabla u \cdot \mathbf{dn}_1 \\
&+ \int_{\partial V_n^2} \phi \underline{D} \nabla u \cdot \mathbf{dn}_2 \\
&+ \int_{\partial V_t^1} \phi \underline{D} \nabla u \cdot \mathbf{dt}_1 \\
&+ \int_{\partial V_t^2} \phi \underline{D} \nabla u \cdot \mathbf{dt}_2 \\
&+ \dots \quad .
\end{aligned} \tag{2.23}$$

The dots indicate that, in the case of three dimensions, there are two more terms for another direction parallel to the boundary $\partial \mathcal{D}$. However, for everything presented in the following, these terms can be treated analogously to the two explicitly mentioned in Eq. (2.23). For a given interface width ξ of ϕ , the normal width of the volume V is chosen such that the two boundaries of V parallel to the boundary $\partial \mathcal{D}$ are at iso- ϕ levels of $\phi = 1 - \varepsilon$ and $\phi = \varepsilon$ for an arbitrarily small $\varepsilon > 0$.

By assuming smooth and bounded solutions u and choosing sufficiently small V (corresponding to small enough ξ for fixed ε), the individual integrands of Eq. (2.23) can be approximated by constants, except for the variation due to the factor ϕ . By then letting ξ tend to zero, i.e. reducing the width of V normal to the boundary $\partial \mathcal{D}$ and making ϕ steeper and steeper, the integral on the left hand side and the integrals of the tangential components ∂V_t^1 and ∂V_t^2 on the right hand side of Eq. (2.23) vanish, because they are integrated over a volume and a surface, respectively, whose size tends to zero. The same is true for the reaction term, which is assumed to be bounded for bounded u . Using the fact that $\phi \approx 1$ on ∂V_n^2 and $\phi \approx 0$ on ∂V_n^1 , only one of the two remaining integrals actually has a non-zero contribution, resulting in

$$0 = \int_{\partial V_n^2} \phi \underline{D} \nabla u \cdot \mathbf{dn}_2 \approx |\partial V_n^2| \underline{D} \nabla u \cdot \mathbf{n} \tag{2.24}$$

$$\Rightarrow \mathbf{n} \cdot \underline{D} \nabla u = 0, \tag{2.25}$$

where $|\partial V_n^2|$ denotes the surface area of ∂V_n^2 .

If the above reasoning was justified, Eq. (2.25) would indicate that no-flux boundary conditions are actually implemented by the phase field method. However, it is not known a priori, whether the integrands are bounded *independent of the choice*

of ξ . As the integrands contain derivatives of u , it is not even sufficient to assume that u is bounded. Indeed, it is quite natural to expect that by letting ξ tend to zero and thus approaching the limit of a non-differentiable ϕ , the gradients of the solution u could blow up. Thus, if the crucial assumption of boundedness is not fulfilled, it can neither be concluded that integrals tend to zero because the integrated volume does, nor that for ∂V_n^1 the approximation $\phi \underline{D}\nabla u = \varepsilon \underline{D}\nabla u \approx 0$ holds (for sufficiently small ε). In fact, it becomes obvious that the line of thoughts above is not sufficient, if one notes that it would also work without the factor ϕ in the volume integrals of Eq. (2.23), which corresponds to the additional prefactor $1/\phi$ in Eq. (2.19). As will be shown below, this prefactor is vital for the method to yield the desired result.

In a more recent publication [29], Li et al. showed that phase-field methods can be used to model a number of different boundary conditions, no-flux being a special case which can indeed implemented by Eq. (2.21). However, the mechanisms described below by which the phase-field method achieves its goal also explain some important details of the numerical implementation not provided by the very abstract proof in Ref. [29].

2.1.5.3 Mechanism of Boundary Condition Enforcement

Rewriting Eq. (2.21), the terms of the original PDE and the influence of the phase field can be separated:

$$\begin{aligned} \frac{\partial u}{\partial t} &= f(u) + \frac{1}{\phi} \nabla \cdot (\phi \underline{D}\nabla u) \\ &= f(u) + \nabla \cdot (\underline{D}\nabla u) + \frac{1}{\phi} (\nabla \phi) \cdot (\underline{D}\nabla u) \end{aligned} \quad (2.26)$$

$$= f(u) + \nabla \cdot (\underline{D}\nabla u) + (\nabla(\ln \phi)) \cdot (\underline{D}\nabla u), \quad (2.27)$$

where “ \cdot ” in the last two equations is the dot product between two vectors. In Eq. (2.27), the third term only becomes active, if there are components of the current density $-\underline{D}\nabla u$ perpendicular to the boundary (i.e. violating the intended no-flux boundary condition), as $\nabla(\ln \phi)$, by definition of the phase field, is just a scaled normal vector:

$$\nabla(\ln \phi) = \frac{\partial \ln \phi}{\partial n} \mathbf{n} \quad (2.28)$$

With this information, Eq. (2.27) reads:

$$\frac{\partial u}{\partial t} = f(u) + \nabla \cdot (\underline{D}\nabla u) + \frac{\partial \ln \phi}{\partial n} \mathbf{n} \cdot (\underline{D}\nabla u) \quad (2.29)$$

Note that the third term resembles an advection term in fluid dynamics, though the velocity field is not divergence free. Shifting \underline{D} to the other side of the scalar product, the velocity field for the quantity u is given by

$$-\frac{\partial \ln \phi}{\partial n} \underline{D} \mathbf{n}. \quad (2.30)$$

As \underline{D} is positive definite, $\mathbf{n} \cdot \underline{D} \mathbf{n} \geq 0$. Taking \mathbf{n} to point out of the domain \mathcal{D} , according to Fig. 2.2c $\partial \ln \phi / \partial n < 0$ holds, which means that the velocity (2.30) points into the same half-space as \mathbf{n} , although it might not be normal to $\partial \mathcal{D}$. Therefore, u is “advected” outwards with a velocity proportional to $|\mathrm{d} \ln \phi / \mathrm{d} n|$.

To show that the assumed boundedness of the integrands in Eq. (2.23) is actually present, the so-called *maximum principle* will be used: If the local reaction term in Eq. (2.21) is ignored for the moment, a pure diffusion equation is obtained. The maximum principle states that the solution $u(\mathbf{x}, t)$ for $0 \leq t < T$ and $\mathbf{x} \in \mathcal{D}_c$ is attained either on the spatial boundary $\partial \mathcal{D}_c$ or at some point $\mathbf{x} \in \mathcal{D}_c$ at $t = 0$ [30]. Another way to say this is: The solution will never exceed the maximum of the initial field u at $t = 0$, provided that the values on the boundary $\partial \mathcal{D}_c$ stay below the maximum as well. The same applies to the minimum. For the purpose of the following reasoning, it is assumed that the boundary $\partial \mathcal{D}_c$ of the auxiliary domain is subject to a passive boundary condition which never attains a maximum or minimum, for example a Dirichlet condition $u = \langle u(t = 0) \rangle_{\mathcal{D}_c}$ on $\partial \mathcal{D}_c$. Below, it will be argued why the boundary condition on the auxiliary domain is not important for the solution u in the physical domain \mathcal{D} .

Having the maximum principle at hand, an upper bound for the left hand side of Eq. (2.23) can be obtained by differentiating Eq. (2.21) (still without the local reaction term) with respect to t and noting that the time derivative $\frac{\partial u}{\partial t}$ itself therefore fulfills the diffusion equation

$$\frac{\partial}{\partial t} \frac{\partial u}{\partial t} = \frac{1}{\phi} \nabla \cdot \left(\phi \underline{D} \nabla \frac{\partial u}{\partial t} \right). \quad (2.31)$$

The initial condition $\left. \frac{\partial u}{\partial t} \right|_{t=0}$ is connected to the initial condition $u_0(\mathbf{x}) = u(\mathbf{x}, t = 0)$ of the original diffusion equation via Eq. (2.21) or (2.29). Given that u_0 fulfills the no-flux boundary condition in the interface region, the ϕ -dependent terms in Eq. (2.29) drop out and thus $\frac{\partial u}{\partial t}$ is bounded independent of ϕ by the maximum principle for all t :

$$\left| \frac{\partial u}{\partial t} \right|_{(\mathbf{x}, t)} \leq C \quad \forall \mathbf{x}, t \quad \text{and} \quad \forall \xi. \quad (2.32)$$

In the context of excitable media, with the source term $f = I_{\text{ion}}$ introducing additional $\frac{\partial u}{\partial t}$ contributions, usually, the fastest time scale of u is given by the rise velocity upon activation. The maximum principle therefore ensures that $\partial u / \partial t$ is not increased

further by the ϕ -dependent diffusion dynamics and C can be interpreted as the upstroke velocity of the action potential.

The boundedness of the integrand involving the reaction term $f(u)$ in Eq. (2.23) is seen immediately, because u itself is subject to a diffusion equation and thus obeying the maximum principle, if $f(u)$ is omitted in Eq. (2.21). Again, this means that the ϕ -dependent diffusion dynamics cannot increase or decrease u further than determined by the reaction dynamics. Therefore u is bounded and so is $f(u)$.

For the remaining terms on the right-hand side of Eq. (2.23), a simpler special case is considered, namely that of a diffusion tensor \underline{D} which is nearly spatially constant in the interface region and of an approximately straight boundary, such that spatial derivatives of \underline{D} and \mathbf{n} can be neglected.⁴ Under these assumptions, differentiating Eq. (2.29) in the normal direction yields:

$$\frac{\partial \frac{\partial u}{\partial n}}{\partial t} = \nabla \cdot \left(\underline{D} \nabla \frac{\partial u}{\partial n} \right) + \frac{\partial \ln \phi}{\partial n} \mathbf{n} \cdot \left(\underline{D} \nabla \frac{\partial u}{\partial n} \right) + \frac{\partial^2 \ln \phi}{\partial n^2} \mathbf{n} \cdot (\underline{D} \nabla u) \quad (2.33)$$

$$= \frac{1}{\phi} \nabla \cdot \left(\phi \underline{D} \nabla \frac{\partial u}{\partial n} \right) + \frac{\partial^2 \ln \phi}{\partial n^2} \mathbf{n} \cdot (\underline{D} \nabla u) \quad (2.34)$$

If only the first term on the right hand side was present, $\frac{\partial u}{\partial n}$ would be bounded by the maximum principle. Due to the shape of the phase field (compare Fig. 2.2 and the beginning of this section), $\frac{\partial^2 \ln \phi}{\partial n^2}$ is negative everywhere in the interface region and approaching zero from below in the outward direction. Therefore, the second term on the right hand side is only present in the interface region and opposite in sign to the normal component of the flux $\underline{D} \nabla u$. As \underline{D} is positive definite, the induced change of $\partial u / \partial n = \mathbf{n} \cdot \nabla u$ leads to a reduction of the normal component of $\underline{D} \nabla u$, because in general, for a vector \mathbf{v} with a normal component v_n

$$\frac{\partial \mathbf{n} \cdot \underline{D} \mathbf{v}}{\partial v_n} = \mathbf{n} \cdot \underline{D} \mathbf{n} \geq 0, \quad (2.35)$$

which means that the change of the normal component of $\underline{D} \mathbf{v}$ is positive, if the normal component of \mathbf{v} is increased. The second term in Eq. (2.34) can therefore be viewed as a feedback term that aims at reducing $\mathbf{n} \cdot \underline{D} \nabla u$ to zero by changing $\mathbf{n} \cdot \nabla u$ appropriately. This can in principle mean that $|\mathbf{n} \cdot \nabla u|$ is increased (if \underline{D} is anisotropic), but zero flux will always be reached at finite values, as indicated above, depending on the parallel components of ∇u . As the phase field transition length ξ

⁴ \underline{D} constant has to be required only in the interface region, because it is reasonable to assume that the dynamical system, uninfluenced by the phase field, only produces finite spatial gradients in the physical domain \mathcal{D} . Anything else would render numerical simulations (even without the phase field method) impossible in any case. Therefore, here, it is sufficient to show that these gradients are not amplified by the choice of the steepness parameter ξ of ϕ . Furthermore, the assumption of a nearly straight boundary is probably not as stringent as it might first seem, as on the spatial scale of ξ , every boundary with finite curvature becomes straight for $\xi \rightarrow 0$. However, this generalization will not be shown here.

tends to zero, the “feedback strength” is increased. Applying the same strategy for the derivative of u parallel to the boundary yields equations for $\mathbf{p} \cdot \nabla u = \partial u / \partial p$ identical to Eq. (2.34), only without the last term. Therefore, this component is bounded by the maximum principle.

In summary, the gradient ∇u will thus be bounded independent of the steepness of the phase field at the boundary of \mathcal{D} (at least in the approximations used here), which renders the line of thoughts after Eq. (2.23) correct. In addition to verifying the validity of the phase field approach, the above reasoning contains some useful information about the mechanisms, by which the no-flux boundary condition is achieved: Most importantly, one ambiguity of the ansatz (2.19) was removed. It is now clear why simply multiplying \underline{D} by the phase-field ϕ does not lead to the desired results, although Eq. (2.23) apparently suggested this. If this was done, Eq. (2.29) would contain $\partial \phi / \partial n$ instead of $\partial \ln \phi / \partial n$ (in addition to a factor ϕ before the diffusion term, which would, however, not have any impact). Replacing $\ln \phi$ by ϕ in Eq. (2.34) would destroy the gradient reduction effect of the second term. Therefore, it would not be possible to conclude that the gradient is bounded.

Furthermore, when the constant C in Eq. (2.32) is interpreted as the upstroke velocity, as suggested, it can be seen from Eq. (2.23) that the accuracy of the method depends on this maximum upstroke velocity. This was also noted in Ref. [26], without, however, taking into account the possibility that this might be caused by the phase field method itself. This has now been ruled out by the line of thoughts above. An additional source of inaccuracy stems from the steepness of gradients arriving at the interface region from inside the domain \mathcal{D} . Equation (2.34) indicates that the boundary condition of the original problem formulated for \mathcal{D} has been replaced by a dynamical process that aims at reducing $\mathbf{n} \cdot (\underline{D} \nabla u)$ to zero. As this does not happen instantaneously, larger initial gradients mean larger remainders of $\mathbf{n} \cdot (\underline{D} \nabla u)$ after the reduction process. In excitable media reaction-diffusion systems, the upstroke velocity and the steepness of gradients are, of course, closely related.

Finally, Eq. (2.29) together with the information illustrated in Fig. 2.2c indicates that the velocity, with which the quantity u is transported outwards, increases steadily in the interface region and becomes $\approx 1/\xi$ after some distance. The smaller ξ , the less information can therefore travel back from $\mathcal{D}_c \setminus \mathcal{D}$ to \mathcal{D} . The only process available for this is the diffusion term in Eq. (2.29), which does not depend on ϕ and is therefore arbitrarily slow. This means that the auxiliary (arbitrary) boundary condition applied for numerical reasons at the boundary $\partial \mathcal{D}_c$ of the auxiliary domain becomes less and less important. This fact is useful for the numerical implementation of the phase field method (see Sect. 2.2.3).

2.1.5.4 Extension to Other Boundary Conditions

Although the phase-field method was designed by Fenton et al. to implement no-flux boundary conditions on arbitrary geometries, with the information above, it can be

extended to a more general type of Neumann boundary conditions of the type

$$\mathbf{n} \cdot \underline{D}\nabla u = \mathbf{n} \cdot \mathbf{E}, \quad (2.36)$$

where \mathbf{E} is a fixed vector. This is a special case of Eq.(2.16), when $\underline{\sigma}_o \nabla v_o$ is a constant electric field vector. It is seen immediately from the line of thoughts after Eq.(2.22) that the corresponding phase field replacement in this case is

$$\nabla \cdot (\underline{D}\nabla u) \rightarrow \frac{1}{\phi} \nabla \cdot (\phi(\underline{D}\nabla u - \mathbf{E})). \quad (2.37)$$

With this substitution, Eq.(2.21) is not altered for regions where $\phi \approx 1$, since $-\nabla \cdot \mathbf{E} = 0$. In the integrals of Eq.(2.23), however, the additional term appears, leading to $\mathbf{n} \cdot (\underline{D}\nabla u - \mathbf{E}) = 0$ in Eq.(2.25), which is the desired boundary condition. The same result can be obtained from Ref. [29] by starting from Eqs.(2.28) and (2.37) and substituting the correct boundary condition.

2.1.6 Models

So far, in this chapter, the cross-membrane current $I_{\text{ion}}(V_m, \mathbf{h})$ in, e.g., Eqs.(2.4), (2.9) or (2.13) has been treated as an unknown quantity whose dynamics is determined by the membrane potential V_m and an additional set of equations for the local (i.e. spatially uncoupled) variables \mathbf{h} . As described in Sect. 2.1.1, one approach to construct this term is to empirically determine the contributions of all different ion species and membrane compounds that lead to transmembrane currents. Indeed, many models based on this *bottom-up approach* exist, although they are by definition based on incomplete data. A comprehensive list of physiological models, ordered by tissue type (atrial/ventricular) and species can be found in Ref. [31]. One advantage of this approach is that model parameters can directly be related to physiological properties, which enables investigations of genetic defects and facilitates the adaption of the model for disease conditions. However, a major drawback of these models is their computational cost, due to the large number of local variables used. One extreme example is the *Wang-Sobie model* for neonatal rat ventricular myocytes [15] with 35 dynamic variables and 74 parameters. Although the large number of parameters might be beneficial for the reasons mentioned above, it is at the same time hindering generic approaches such as parameter scans or fitting procedures. Also, for most physiological models, sensitivity of the dynamics to individual parameters is not documented, which further complicates the analysis.

On the other end of the spectrum, generic models are created using a *top-down approach* to the model construction problem. Rather than incorporating every possible detail of the system for which information exists, they try to mimic the basic properties of cardiac tissue (or even more generic: of excitable media) using the

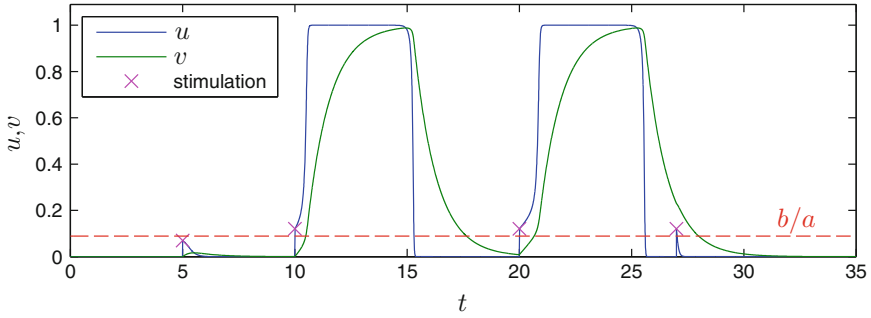


Fig. 2.4 Barkley model dynamics. Four attempts, marked by “x”, to induce an excitation in the Barkley model (without diffusion) by instantaneously setting the model variable u . In the first case, the stimulation is subthreshold. The second and third stimulation produce almost identical excitations, whereas the fourth stimulation occurs at a time when excitability is not fully recovered yet, as v has not returned to zero. Because of this refractoriness, the stimulation fails to produce an excitation. Model parameters: B1 (see Table A.1, p. 184)

fewest number of variables and parameters possible to achieve a particular degree of realism. A very generic model for excitable media is the *Barkley model* [32], which consists of only two variables and three parameters which determine the basic properties of the medium such as the excitability, excitation threshold and duration. The Barkley model will be used in this work for numerical simulations, when values of physiological parameters are not important or unknown and when results are to be obtained for the large class of excitable media. In all other simulations, the somewhat more detailed three-variable *Fenton-Karma model* [33] will be used, which has 14 parameters that enable it to reproduce important aspects of the dynamics of more realistic cardiac models.

2.1.6.1 The Barkley and the Bär-Eiswirth Model

This two-variable, generic model was developed by Barkley in the beginning of the 1990s in an effort to understand spiral wave dynamics in generic excitable media. Although already used in Ref. [32], it was newly introduced in its most efficient numerical form in Ref. [34]. Its equations are

$$\frac{\partial u}{\partial t} = \frac{1}{\epsilon} u(1-u) \left(u - \frac{v+b}{a} \right) + \nabla^2 u \quad (2.38a)$$

$$\frac{\partial v}{\partial t} = g(u, v), \quad (2.38b)$$

with the parameters ϵ , a and b . For the original Barkley model, $g(u, v) = u - v$. The fast variable u can be identified as a normalized V_m in the mono-domain formalism of Sect. 2.1.3, while the local part on the right hand side of the u -equation represents

the cross-membrane current term $-I_{\text{ion}}/C_m$. There is only one local variable, such that \mathbf{h} is actually a scalar and $h = v$. The diffusion tensor is normalized to $\underline{D} = \text{Id}$. An example of the local dynamics of the model, i.e. without the diffusion term, following a series of stimulations is shown in Fig. 2.4. It can be understood from the (u, v) phase space structure, which is typical for simple excitable systems⁵ and is depicted in Fig. 2.5. It has a stable fixed point at $(0, 0)$, whose basin of attraction is the whole square $[0, 1] \times [0, 1]$, but trajectories starting a considerable distance⁶ right of the nullcline $u = (v + b)/a$ make a large detour close to $u = 1$, $v = 1$ and $v = 0$ before returning to the fixed point. In contrast, trajectories starting close to $(u, v) = (0, 0)$ return directly. The first case corresponds to action potential following a superthreshold depolarization, whereas the second is a subthreshold depolarization not strong enough to evoke an action potential. The meaning of the three parameters in terms of the characteristics of excitable media can readily be read off the phase space diagram: b/a is the excitation threshold during rest, whereas ϵ determines the time scale of u compared to v . Its main impact is on the *upstroke velocity* of an action potential, which also determines the conduction velocity in the spatially extended case in conjunction with diffusion. a on its own mainly influences the action potential duration, as it determines the slope of the above-mentioned nullcline and thus the value of v at which u starts to decrease.

Despite its simplicity, the Barkley model (now, again, including the Laplacian term) supports a large number of different wave patterns, including pulses, plane waves and both stationary and meandering spiral waves. However, there are no (homogeneous) parameters for which the Barkley displays spiral wave breakup or other types of chaos. It was shown by Bär and Eiswirth that turbulence can be observed by delaying the increase of the slow variable v . This can be done by redefining g in Eq. (2.38b) as follows [37]:

$$g(u, v) = \begin{cases} -v & u < \frac{1}{3} \\ 1 - 6.75u(u - 1)^2 - v & \frac{1}{3} \leq u \leq 1 \\ 1 - v & u \geq 1 \end{cases} \quad (2.39)$$

This modification will be referred to as the *Bär-Eiswirth model* in the rest of this thesis.

⁵ Another example for a two-variable system with a similar phase space structure is the FitzHugh-Nagumo model [35, 36], which is a reduced version of the nerve axon model constructed by Hodgkin and Huxley.

⁶ This distance is indeed finite and depends on the parameter ϵ , which determines, for a fixed starting point of the trajectory, whether the u dynamics will be successful in driving the system even more to the right and thus to performing an action potential, or whether the v dynamics is dominant and brings the system back over the u -nullcline and thus directly to the fixed point.

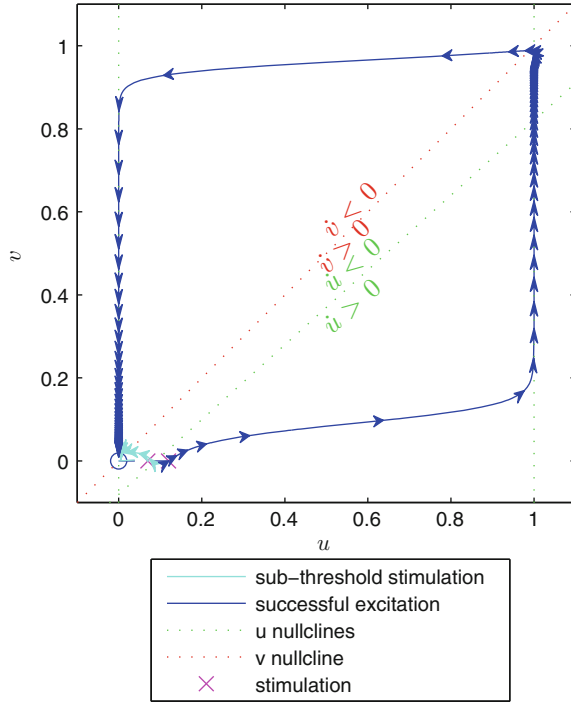


Fig. 2.5 Barkley model: local phase space. Shown are two stimulation attempts from the fully recovered state: one is subthreshold (cyan), causing the system to return immediately to the stable fixed point at $(0,0)$, whereas the other one is far enough in the $\dot{u} > 0$ region to produce an excitation (blue). Arrows on the trajectories mark equidistant time points, indicating the fast dynamics of u compared to v . The tilted u nullcline has the equation $v = au - b$ and is responsible for the refractoriness shortly after an excitation, when still $v > 0$, but $u \approx 0$: in this case, the distance to the right necessary to cross the u nullcline is considerably increased. When $v > a - b$, the system is in absolute refractoriness, because then for every $u \in [0, 1[$ it is $\dot{u} < 0$. Model parameters: B1 (see Table A.1, p. 184)

2.1.6.2 The Fenton-Karma Model

The equations for this generic model were developed by Fenton and Karma in 1998 with the aim of capturing the most important features specific to cardiac models (as opposed to general excitable media). Consequently, although the model has only three variables, it is considerably more tightly connected to the physiological mechanisms of excitability in the cardiac muscle. The model considers three cross-membrane currents, named fast inward (fi), slow outward (so) and slow inward (si) current. These roughly correspond to the sodium, potassium and calcium currents, respectively (cf. Sect. 1.2.1). However, the complexity of different ion channel types and other contributions to membrane potential dynamics has been condensed into these net currents and their activation and inactivation. Therefore, the parameters (most of

which are timescales and thresholds) have a physiological meaning in that they reflect typical or net properties of these summarized currents, but nevertheless they cannot be interpreted as descriptions of the microscopic components responsible for membrane potential dynamics.

The equations of the Fenton-Karma model are

$$\frac{\partial u}{\partial t} = \nabla \cdot \underline{D} \nabla u - J_{\text{fi}}(u, v) - J_{\text{so}}(u) - J_{\text{si}}(u, w) \quad (2.40a)$$

$$\frac{\partial v}{\partial t} = \Phi(u_c - u)(1 - v) \left(\frac{\Phi(u - u_v)}{\tau_{v1}^-} + \frac{\Phi(u_v - u)}{\tau_{v2}^-} \right) - \Phi(u - u_c) \frac{v}{\tau_v^+} \quad (2.40b)$$

$$\frac{\partial w}{\partial t} = \Phi(u_c - u) \frac{1 - w}{\tau_w^-} - \Phi(u - u_c) \frac{w}{\tau_w^+} \quad (2.40c)$$

where the three cross-membrane currents are defined as

$$J_{\text{fi}}(u, v) = -\frac{v}{\tau_d} \Phi(u - u_c)(1 - u)(u - u_c) \quad (2.41a)$$

$$J_{\text{so}}(u) = \frac{u}{\tau_0} \Phi(u_c - u) + \frac{1}{\tau_r} \Phi(u - u_c) \quad (2.41b)$$

$$J_{\text{si}}(u, w) = -\frac{w}{2\tau_{\text{si}}} (1 + \tanh[k(u - u_c^{\text{si}})]). \quad (2.41c)$$

The sum of these currents corresponds to the term $-I_{\text{ion}}/C_m$ of Sect. 2.1.3. Again, u is a normalized membrane potential V_m and on the order 0 to 1, such that one unit of u roughly corresponds to a 100 mV membrane potential change. The vector of local variables for the Fenton-Karma model therefore is $\mathbf{h} = (v, w)$.

In its original published form, the function $\Phi(x)$ in Eqs. (2.40) and (2.41) is simply the step function

$$\Phi(x) = \Theta(x) := \begin{cases} 1 & x \geq 0 \\ 0 & x < 0. \end{cases} \quad (2.42)$$

However, in this case, the right hand side of the dynamical system (2.40) is not differentiable. When this is required, a continuous approximation for the step function will be used instead:

$$\Phi(x) = \Theta^*(x) := \frac{1}{2}(1 + \tanh(k_2 x)) \quad (2.43)$$

In this way, k_2 becomes an additional parameter of the model and the original dynamics is recovered for $k_2 \rightarrow \infty$, which is why large values for k_2 will be used throughout this thesis. With this choice of Φ , the equations will be referred to as the *smooth Fenton-Karma model*.

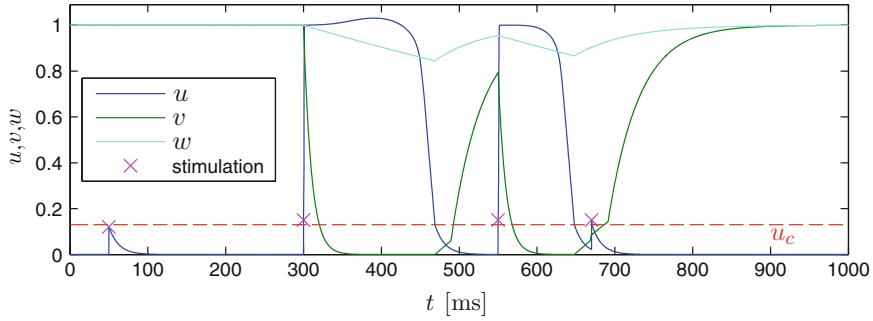


Fig. 2.6 Fenton-Karma model dynamics. Four attempts, marked by “x”, to induce action potentials in the Fenton-Karma model (without diffusion) by instantaneously setting the model variable u . In the first case, the stimulation is subthreshold. The second and third stimulation each produce an excitation, but the APD varies due to restitution. The fourth stimulation occurs during refractoriness and fails to produce an action potential. Model parameters: FK1 (see Table A.2, p. 184)

The steady state of the Fenton-Karma model is close to $(u, v, w) \approx (0, 1, 1)$, where u , even for the case $\Phi = \Theta$, deviates slightly from 0 because of the tanh term in Eq. (2.41c). If depolarized above the threshold u_c , the fast inward current J_{fi} drives u rapidly towards 1, on a time scale defined by τ_d . J_{so} is responsible for repolarization, whereas J_{si} is the current that counteracts J_{so} during the plateau phase [33]. The local variables v and w are gates for the fast and slow inward currents, respectively. For the resting state, these two currents have their full amplitude, but time periods in which $u > u_v$ or $u > u_c$ bring v and w closer to 0, thereby reducing the ability of the model membrane to depolarize or withstand the repolarizing slow outward current. This leads to both a decrease in membrane excitability (upstroke velocity) and *action potential duration* (APD), the former correlating with *conduction velocity* (CV).

As both kinds of refractoriness are parameterized separately with corresponding thresholds and time scales, the Fenton-Karma model is able to reproduce a variety of CV and APD restitution curves, even for more complex models as well as experimentally measured restitution curves. Indeed, providing a simple (as opposed to ionically accurate) model with realistic restitution properties was one of the primary reasons for its construction [33]. Later, an extended version with four variables was published which, in addition to the restitution properties, also produces more accurate action potential shapes [28]. In summary, despite its lack of detail on the ionic level, the Fenton-Karma model represents an intermediate class of models that is still generic but accounts for some important properties specific to cardiac tissue. An example trajectory of the local model dynamics is shown in Fig. 2.6. It should be noted that the meaning of the parameters τ_{v1}^- and τ_{v2}^- is reversed in Ref. [38] with respect to the original model publication in Ref. [33]. In this work, the original definition is used.

2.1.7 Spiral Tips and Phase Singularities

In contrast to plane waves which travel through a given finite domain only once and self-terminate when they arrive at a boundary, spiral waves have, in principle, an unlimited life span. Both the Barkley model and the Fenton-Karma model can exhibit this fundamental excitation pattern of excitable media. The inherent stability of spiral waves is one of the key reasons for their dangerousness in the context of cardiac dynamics (see Sect. 1.4). Even during the chaotic activity of fibrillation, activity has been shown to be organized around phase singularities [39, 40].

Spiral waves can, in general, extend over an arbitrarily large domain. However, unless the spiral is perturbed very close to its center (the *spiral tip*), it will continue to rotate largely uninfluenced. The organizing centers around which spiral waves rotate can be characterized by *phase singularities*. A suitable phase for the detection of phase singularities can be defined in different ways. In the two-variable Barkley model, this is particularly simple, since the trajectory of a normal activation in the local phase space is similar enough to a circle to define a phase θ by the function [41]

$$\theta(\mathbf{x}, t) = \arctan2(u(\mathbf{x}, t) - u^*, v(\mathbf{x}, t) - v^*), \quad (2.44)$$

where (u^*, v^*) is a point in the local phase space which is circled by the trajectory during a normal activation. For the example shown in Fig. 2.5, $(u^*, v^*) = (0.3, 0.3)$ would be an appropriate choice, although one has to ensure that the values are still adequate when looking at the dynamics of a single point embedded into the extended system. An example for this definition of the phase and the resulting phase distribution in space are shown in Fig. 2.7 for a spiral wave in the Barkley model. Close to the center of the domain, all different phases $\theta \in]-\pi, \pi]$ are present. This point defines the phase singularity. When the model has more than two variables, one can select two suitable variables or two different combinations of variables to define the phase according to Eq. (2.44). If this is not straightforward or, e.g., only the membrane potential is available experimentally, delay embeddings (or, almost equivalently, the derivative) of the membrane potential or Hilbert transformations can be used to obtain a second variable for the definition of a phase [41–43]. In this thesis, spiral tip detection will only be carried out for the Barkley model, so the above method is sufficient.

In a spatial domain \mathcal{D} with two dimensions and with a suitable definition of the phase, the *topological charge* n^{top} can be defined as [44]

$$n^{\text{top}} = \frac{1}{2\pi} \oint_{\partial\mathcal{D}} \nabla\theta \, d\mathbf{l}, \quad (2.45)$$

where \mathbf{l} is the path parameterizing the boundary $\partial\mathcal{D}$ of \mathcal{D} . $\nabla\theta$ is well-defined (except at the phase singularity itself) if the phase interval $]-\pi, \pi]$ is interpreted as having periodic boundary conditions, or equivalently, if for each point in space, the branches of the $\arctan2$ function are chosen appropriately. Assuming that the phase θ is differentiable everywhere in \mathcal{D} , Eq. (2.45) trivially yields $n^{\text{top}} = 0$ due to Stokes' theorem.

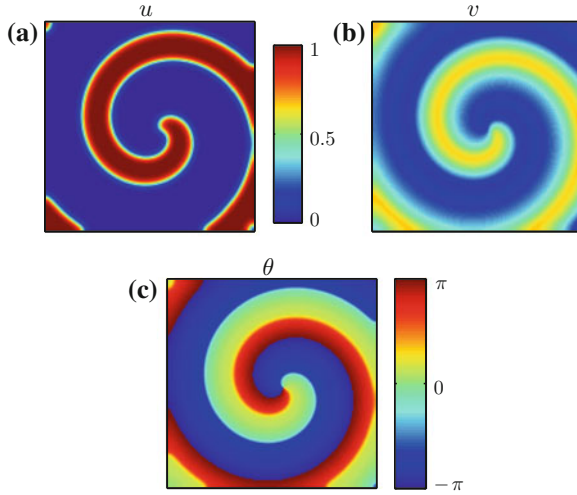


Fig. 2.7 Spatial phase distribution. **a, b** Exemplary distributions of the u and v variables of the Barkley model during spiral wave dynamics. **c** Distribution of the phase θ . Near the center of the domain, all phases converge in a single point—the phase singularity. Simulation of the Barkley model using parameter set B1 (see Table A.1, p. 184)

However, integrating once around a phase singularity leads to a line integral of $\pm 2\pi$, which is possible despite Stokes' theorem, because θ cannot be made differentiable everywhere. The topological charge of a domain with one phase singularity is thus $n^{\text{top}} = \pm 1$, where the sign indicates the chirality of the phase singularity, which, for the same definition of the phase, characterizes the direction of rotation of the spiral wave. If multiple phase singularities are present in the domain within the integration path, a net topological charge is obtained. For the sake of detecting spiral tips, therefore, small integration domains have to be chosen (see numerical implementation of spiral tip detection in Sect. 2.2.5).

It should be noted that there are other ways of finding spiral wave tips which do not rely on the definition of a phase. One possibility is to find the intersection of the iso-lines for two different variables. These two variables can either be two model variables or a second variable can be obtained using one of the methods mentioned above. A common choice for the detection of spiral tips and their three-dimensional equivalents, *filaments* of scroll waves, is \dot{V}_m as the second iso-line or iso-surface (see Appendix B of Ref. [33]). However, these methods of intersection do not reveal any information about the chirality of the spiral waves.

2.1.8 Lyapunov Stability Analysis

Let

$$\frac{d\mathbf{u}}{dt} = \mathbf{f}(\mathbf{u}) \quad \text{with} \quad \mathbf{u}(t_0) = \mathbf{u}_0 \quad (2.46)$$

be a bounded, continuous dynamical system⁷ with differentiable $\mathbf{f} : \mathbb{R}^n \rightarrow \mathbb{R}^n$ and $\mathbf{u} \in \mathbb{R}^n$, where n is the phase space dimension. Lyapunov stability analysis can make a statement about overall stability properties of an attractor and quantifies the “sensitive dependence on initial conditions” that is often viewed as a defining criterion for chaos. This is done by analyzing the behavior of small perturbations with respect to a reference trajectory under the assumption that the system is ergodic. An attractor is regarded as stable, when perturbations in arbitrary directions in phase space do not, in the long run, grow with time, i.e. all perturbed trajectories decay back to the reference trajectory or at least do not diverge from it. The analysis is carried out in the tangent space of the dynamics, i.e. up to linear order. As will be described below in detail, this approximation in general leads to different exponential growth rates in distinct directions in tangent space, i.e. a perturbation $\delta\mathbf{u}$ initialized at time t_0 grows approximately like $\delta\mathbf{u}(t_0 + t) = \delta\mathbf{u}(t_0) \exp(\lambda t)$ for large t . The growth rate λ , which depends on direction of the initial perturbation, is the so-called Lyapunov exponent associated with this direction. The scenario for a specific direction in phase space is illustrated in Fig. 2.8. Note, however, that in reality, the behavior of the perturbations can vary substantially across different regions of the attractor. Lyapunov exponents are therefore long-term, average growth rates.

In the following, a very condensed summary of the mathematical definition of Lyapunov exponents and vectors will be given, facilitating the numerical implementation of the analysis (see Sect. 2.2.6) and the interpretation of the results in Sect. 3.1. Instead of working through this rather technical and mathematical section, some readers might prefer to skip directly to the next section (p. 57) and obtain a more intuitive understanding of the meaning of Lyapunov exponents and vectors while reading the results in Sect. 3.1.

2.1.8.1 Definition of Lyapunov Exponents

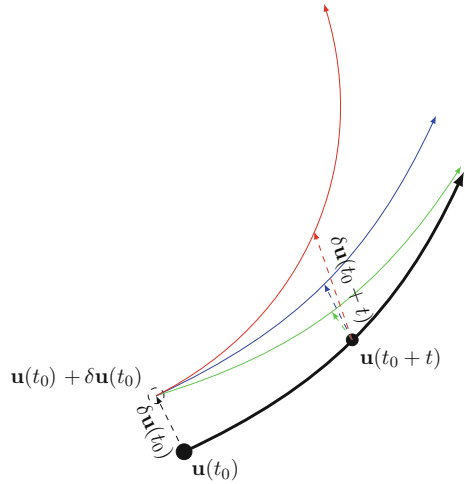
Let

$$\Phi^t : (t, \mathbf{u}_0) \mapsto \mathbf{u}(t_0 + t) \quad (2.47)$$

$$\mathbb{R} \times \mathbb{R}^n \rightarrow \mathbb{R}^n$$

⁷ In allusion to some of the excitable media models used in this thesis, the letter \mathbf{u} refers here to a state in phase space (instead of the more widely-used \mathbf{x}) to avoid confusion with a position $\mathbf{x} \in \mathbb{R}^d$ in space (with $d = 1, 2, 3$).

Fig. 2.8 Lyapunov stability analysis extracts growth rates of perturbations. The *black line* represents a reference trajectory $\mathbf{u}(t_0 + t)$, which is a solution of the dynamical system. An infinitesimally perturbed initial condition (*dashed circle*) leads to different trajectories. On average, for $t \rightarrow \infty$, the perturbation $\delta\mathbf{u}$ with respect to the reference trajectory either shrinks exponentially (*green line*; $\lambda < 0$), stays constant (*blue line*; $\lambda = 0$) or grows exponentially (*red line*; $\lambda > 0$)



be the flow of the system, where the first argument t is usually written as a superscript and which is alternatively understood as a family of functions $\Phi^t : \mathbb{R}^n \rightarrow \mathbb{R}^n$ parametrized by t . Combining Eqs. (2.46) and (2.47), this definition is equivalent to the statement

$$\left. \frac{\partial \Phi^t}{\partial t} \right|_{t'} = \mathbf{f} \circ \Phi^{t'} \quad \text{with} \quad \Phi^0 = \text{Id}_{\mathbb{R}^n}. \quad (2.48)$$

Given a reference trajectory $\mathbf{u}(t_0 + t)$, we can ask how an infinitesimally perturbed trajectory with an initial condition $\mathbf{u}_0 + \delta\mathbf{u}_0$ instead of \mathbf{u}_0 evolves. Up to linear order the following identity holds

$$\frac{\partial \delta\mathbf{u}}{\partial t} = \frac{\partial(\mathbf{u} + \delta\mathbf{u})}{\partial t} - \frac{\partial\mathbf{u}}{\partial t} = \mathbf{f}(\mathbf{u} + \delta\mathbf{u}) - \mathbf{f}(\mathbf{u}) \approx \mathbf{f}(\mathbf{u}) + \mathbf{J}_{\mathbf{f}}^{\mathbf{u}} \delta\mathbf{u} - \mathbf{f}(\mathbf{u}) = \mathbf{J}_{\mathbf{f}}^{\mathbf{u}} \delta\mathbf{u}, \quad (2.49)$$

where $\mathbf{J}_{\mathbf{f}}^{\mathbf{u}}$ denotes the Jacobian of \mathbf{f} at the point $\mathbf{u} \in \mathbb{R}^n$. Alternatively, we can use the flow with the perturbed initial condition to obtain an approximation for the temporal evolution of the perturbation $\delta\mathbf{u}$:

$$\begin{aligned} \delta\mathbf{u}^*(t_0 + t) &= \mathbf{u}(t_0 + t) + \delta\mathbf{u}^*(t_0 + t) - \mathbf{u}(t_0 + t) \\ &= \Phi^t(\mathbf{u}_0 + \delta\mathbf{u}_0) - \Phi^t(\mathbf{u}_0) \approx \mathbf{J}_{\Phi^t}^{\mathbf{u}_0} \delta\mathbf{u}_0 \end{aligned} \quad (2.50)$$

To see that Eq. (2.50) actually describes the same dynamics as Eq. (2.49), we expand the time derivative of $\mathbf{J}_{\Phi^t}^{\mathbf{u}_0}$. Assuming all the partial derivatives of the flow are continuous and thus commute, we have

$$\left. \frac{\partial \mathbf{J}_{\Phi^t}^{\mathbf{u}_0}}{\partial t} \right|_{t'} = \mathbf{J}_{\frac{\partial \Phi}{\partial t}}^{\mathbf{u}_0} \stackrel{(2.48)}{=} \mathbf{J}_{\mathbf{f} \circ \Phi^{t'}}^{\mathbf{u}_0} = \mathbf{J}_{\mathbf{f}}^{\Phi^{t'}(\mathbf{u}_0)} \circ \mathbf{J}_{\Phi^{t'}}^{\mathbf{u}_0} = \mathbf{J}_{\mathbf{f}}^{\mathbf{u}(t_0+t')} \circ \mathbf{J}_{\Phi^{t'}}^{\mathbf{u}_0}. \quad (2.51)$$

The composition operator \circ for linear maps was deliberately used in the last two steps instead of ordinary matrix multiplication to emphasize the similarity of Eq. (2.48)–(2.51). A straightforward calculation shows that $\mathbf{J}_{\Phi^0}^{\mathbf{u}_0} = \text{Id}_{\mathbb{R}^n}$. By comparing Eq. (2.48) with (2.46) and in the same way Eq. (2.51) with (2.49), we see that $\mathbf{J}_{\Phi^t}^{\mathbf{u}_0}$ is indeed the flow for the perturbations defined by Eq. (2.49), i.e.

$$\delta \mathbf{u}^*(t) = \delta \mathbf{u}(t). \quad (2.52)$$

Oseledec's theorem [45] ensures under fairly general conditions that the limit

$$\lim_{t \rightarrow \infty} (\mathbf{J}_{\Phi^t}^{\mathbf{u}_0 T} \mathbf{J}_{\Phi^t}^{\mathbf{u}_0})^{1/2t} = \Lambda_{\mathbf{u}_0} \quad (2.53)$$

exists for almost all initial conditions \mathbf{u}_0 on the attractor. The logarithms of the eigenvalues of Λ are called Lyapunov exponents and are denoted by $\lambda_i, i = 1, \dots, n$, with the convention that $\lambda_i \geq \lambda_j$ for $i < j$. If we denote the unique Lyapunov exponents (i.e. without multiplicity) by $\lambda^{(i)}$, each of them is associated with the eigenspace $E^{(i)}$ belonging to the eigenvalue $\exp(\lambda^{(i)})$, where $\dim E^{(i)}$ is the multiplicity of the Lyapunov exponent. In this alternative definition, i ranges between 1 and \tilde{n} , where \tilde{n} is the number of distinct Lyapunov exponents. One of the fundamental properties of Lyapunov exponents which makes them useful for the characterization of attractors is that, for ergodic systems, the eigenvalues of $\Lambda_{\mathbf{u}_0}$ and thus the Lyapunov exponents are identical for almost all⁸ initial conditions \mathbf{u}_0 and only the matrix itself and its eigenvectors really depend on \mathbf{u}_0 . Oseledec also showed that these exponents can be obtained by looking at the linearized dynamics of single perturbations $\delta \mathbf{u}$, which are initialized in the right subset of tangent space:

$$\lambda^{(i)} = \lim_{t \rightarrow \infty} \frac{1}{t} \ln \|\mathbf{J}_{\Phi^t}^{\mathbf{u}_0} \delta \mathbf{u}_0\| \quad \delta \mathbf{u}_0 \in \mathfrak{E}^{(i)} \setminus \mathfrak{E}^{(i+1)} \subset \mathbb{R}^n \quad (2.54)$$

$\mathfrak{E}^{(i)}$ is the subspace of \mathbb{R}^n which is spanned by eigenvectors for which $\lambda \leq \lambda^{(i)}$:

$$\mathfrak{E}^{(i)} = \text{span}(E^{(i)}, E^{(i+1)}, \dots, E^{(\tilde{n})})$$

and for consistency we define $\mathfrak{E}^{(\tilde{n}+1)} := \{0\}$. Let $U^p \in \mathbb{R}^n$ be an arbitrary set which is contained and open in the p -dimensional subspace spanned by linearly independent vectors $\delta \mathbf{u}_0^{r_k} \in \mathfrak{E}^{(r_k)} \setminus \mathfrak{E}^{(r_k+1)}$ for $1 \leq k \leq p$ and r_k suitable integer numbers. As an extension of Eq. (2.54), it can be shown that U^p grows like the sum of the corresponding Lyapunov exponents [46–48]:

⁸ Exceptions are, e.g., unstable fixed points or unstable periodic orbits embedded into an attractor.

$$\lim_{t \rightarrow \infty} \frac{1}{t} \ln \text{Vol}(\mathbf{J}_{\Phi^t}^{\mathbf{u}_0} U^p) = \sum_{k=1}^p \lambda^{(r_k)} \quad (2.55)$$

Since the actual choice of U^p within the subspace does not matter, for simplicity, one can think of the parallelotope spanned by the $\delta \mathbf{u}_0^{r_k}$. Choosing $\text{Vol}(U^p) = 1$ is a convenient choice to assign $\text{Vol}(\mathbf{J}_{\Phi^t}^{\mathbf{u}_0} U^p)$ the meaning of a growth factor even for finite t . Note however that, in the formulation of Eqs. (2.54) and (2.55), the choice of $\delta \mathbf{u}_0$ or the $\delta \mathbf{u}_0^{r_k}$ requires a-priori knowledge of the subspaces $E^{(i)}$. Guessing these subspaces for all Lyapunov exponents but the first ($i = 1$) is nearly impossible because $\mathfrak{E}^{(i)}$ has zero-measure in \mathbb{R}^n for $i > 1$. Besides this systematic problem, numerical calculation is impeded by the fact that slight numerical errors will always lead to components of $\delta \mathbf{u}$ in $\mathfrak{E}^{(1)} \setminus \mathfrak{E}^{(2)}$, which composes almost all of \mathbb{R}^n . Therefore, any (even most carefully chosen) $\delta \mathbf{u}_0$ will asymptotically grow like $\exp(\lambda_1 t)$.

In 1980, more than a decade after the rigorous mathematical definition of Lyapunov exponents by Oseledec [45], Benettin and co-workers found a method for calculating all Lyapunov exponents [49, 50]. It makes use of two basic facts: Firstly, assuming $t = t(m) = m\Delta t$ with some $m \in \mathbb{N}$, the Jacobian $\mathbf{J}_{\Phi^t}^{\mathbf{u}_0}$ can be replaced by

$$\mathbf{J}_{\Phi^t}^{\mathbf{u}_0} = \mathbf{J}_{\Phi^{\Delta t}}^{\mathbf{u}(t_0+(m-1)\Delta t)} \mathbf{J}_{\Phi^{\Delta t}}^{\mathbf{u}(t_0+(m-2)\Delta t)} \dots \mathbf{J}_{\Phi^{\Delta t}}^{\mathbf{u}_0}. \quad (2.56)$$

Secondly, like almost any $\delta \mathbf{u}_0$ will be in $\mathfrak{E}^{(1)} \setminus \mathfrak{E}^{(2)}$, similarly, almost any p -dimensional parallelotope U^p defined by linearly independent $\delta \mathbf{u}_0^k$, $1 \leq k \leq p$ will be in $\mathfrak{E}^{(1)} \setminus \mathfrak{E}^{(p^*+1)}$, where p^* is chosen such that $\lambda^{(p^*)} = \lambda_p$. This means that, almost certainly, the r_k in Eq. (2.55) refer to the p most expanding directions:

$$\lim_{t \rightarrow \infty} \frac{1}{t} \ln \text{Vol}(\mathbf{J}_{\Phi^t}^{\mathbf{u}_0} U^p) = \sum_{k=1}^p \lambda_k \quad (2.57)$$

Since we are dealing with linear maps and so the volume of all open sets in a subspace grows by the same factor, by virtue of Eq. (2.56), growth of the subspace $\text{span}(\delta \mathbf{u}_0^1, \delta \mathbf{u}_0^2, \dots, \delta \mathbf{u}_0^p)$ can be calculated as

$$\begin{aligned} \text{Vol}(\mathbf{J}_{\Phi^t}^{\mathbf{u}_0} U^p) &= \text{Vol}(\mathbf{J}_{\Phi^{\Delta t}}^{\mathbf{u}(t_0+(m-1)\Delta t)} U_{m-1}^p) \cdot \text{Vol}(\mathbf{J}_{\Phi^{\Delta t}}^{\mathbf{u}(t_0+(m-2)\Delta t)} U_{m-2}^p) \dots \text{Vol}(\mathbf{J}_{\Phi^{\Delta t}}^{\mathbf{u}_0} U^p) \\ &= \prod_{l=0}^{m-1} \text{Vol}(\mathbf{J}_{\Phi^{\Delta t}}^{\mathbf{u}(t_0+l\Delta t)} U_l^p) \quad \text{with } U_0^p := U^p, \end{aligned} \quad (2.58)$$

where the parallelotopes fulfill $\text{Vol}(U_i^p) = 1$ for $1 \leq i \leq m-1$ and the $\delta \mathbf{u}_i^k$, $1 \leq k \leq p$ spanning the parallelotope U_i^p satisfy

$$\begin{aligned} &\text{span}(\delta \mathbf{u}_{i+1}^1, \delta \mathbf{u}_{i+1}^2, \dots, \delta \mathbf{u}_{i+1}^p) \\ &\equiv \text{span}(\mathbf{J}_{\Phi^{\Delta t}}^{\mathbf{u}(t_0+i\Delta t)} \delta \mathbf{u}_i^1, \mathbf{J}_{\Phi^{\Delta t}}^{\mathbf{u}(t_0+i\Delta t)} \delta \mathbf{u}_i^2, \dots, \mathbf{J}_{\Phi^{\Delta t}}^{\mathbf{u}(t_0+i\Delta t)} \delta \mathbf{u}_i^p). \end{aligned} \quad (2.59)$$

The latter means that a suitable parallelotope can be chosen for each step of the linearized flow independently, as long as the new parallelotope is in the same subspace as the result from the last step ($\text{Vol}(U_i^p) = 1$ was only chosen to avoid having to divide by the original volume in each step to obtain the growth factor).

As noted by Benettin, a convenient way to calculate the parallelotopes' volume and get a computationally favorable representation of the subspaces is by means of a reduced *QR-decomposition*: Let $\mathbf{A}^{i+1} \in \mathbb{R}^{n \times p}$ be a matrix whose columns are the p linearly independent vectors spanning the parallelotope $\mathbf{J}_{\Phi \Delta t}^{\mathbf{u}(t_0+i\Delta t)} U_i^p$. $\mathbf{A}^{i+1} = \mathbf{Q}^{i+1} \mathbf{R}^{i+1}$ is a unique decomposition of \mathbf{A}^{i+1} into a matrix $\mathbf{Q}^{i+1} \in \mathbb{R}^{n \times p}$ whose columns are orthonormal and an upper triangular matrix $\mathbf{R}^{i+1} \in \mathbb{R}^{p \times p}$ whose diagonal elements we require to be positive. Each column of \mathbf{A}^{i+1} is thus expressed as a linear combination of the columns of \mathbf{Q}^{i+1} whose weights are given by the corresponding column of \mathbf{R}^{i+1} . As \mathbf{R}^{i+1} is upper triangular, the first q columns of \mathbf{Q}^{i+1} ($1 \leq q \leq p$) span the same subspace as the first q columns of \mathbf{A}^{i+1} . Therefore, for any dimension q , $1 \leq q \leq p$, the first q columns of \mathbf{Q}^{i+1} can be chosen as a replacement (according to Eq.(2.59)) for the parallelotope $\mathbf{J}_{\Phi \Delta t}^{\mathbf{u}(t_0+i\Delta t)} U_i^q$ spanned by the first q columns of \mathbf{A}^{i+1} . Applying the linearized flow to the parallelotopes U_i^p as in Eq.(2.58) therefore corresponds to a matrix multiplication $\mathbf{A}^{i+1} = \mathbf{J}_{\Phi \Delta t}^{\mathbf{u}(t_0+i\Delta t)} \mathbf{Q}^i$.

The new parallellotopes for the next step given by \mathbf{Q}^{i+1} automatically fulfill $\text{Vol}(U_{i+1}^p) = 1$. Since the columns of \mathbf{Q}^{i+1} are orthonormal, the q -dimensional volume of the parallelotope given by the first q columns of \mathbf{A}^{i+1} can be calculated using

$$\text{Vol}(\mathbf{J}_{\Phi \Delta t}^{\mathbf{u}(t_0+i\Delta t)} U_i^q) = \prod_{j=1}^q R_{jj}^{i+1}. \quad (2.60)$$

Putting it all together, we have

$$\begin{aligned} \sum_{k=1}^q \lambda_k &= \lim_{t \rightarrow \infty} \frac{1}{t} \ln \text{Vol}(\mathbf{J}_{\Phi t}^{\mathbf{u}_0} U^q) \stackrel{(2.58)}{=} \lim_{m \rightarrow \infty} \frac{1}{m \Delta t} \sum_{l=0}^{m-1} \ln \text{Vol}(\mathbf{J}_{\Phi \Delta t}^{\mathbf{u}(t_0+l\Delta t)} U_l^q) \\ &= \lim_{m \rightarrow \infty} \frac{1}{m \Delta t} \sum_{l=0}^{m-1} \sum_{j=1}^q \ln R_{jj}^{l+1} = \lim_{m \rightarrow \infty} \frac{1}{m \Delta t} \sum_{l=1}^m \sum_{j=1}^q \ln R_{jj}^l. \end{aligned} \quad (2.61)$$

By subtracting both sides of Eq.(2.61) for $q = i$ and $q = i - 1$, it becomes clear that the Lyapunov exponents are just the time-averaged logarithms of the individual diagonal elements of \mathbf{R} :

$$\lambda_i = \lim_{m \rightarrow \infty} \frac{1}{m \Delta t} \sum_{l=1}^m \ln R_{ii}^l \quad (2.62)$$

2.1.8.2 Norm-independence and Covariance

Lyapunov exponents are independent of the norm (and scalar product) and of the starting point \mathbf{u}_0 (except for some zero-measure set) on the attractor [45, 47, 48]. This makes them a property of the dynamical system itself, or, more specifically, of one attractor of it, invariant under diffeomorphic coordinate transformations. The same applies to the subspaces $\mathfrak{E}^{(1)} \supset \mathfrak{E}^{(2)} \supset \dots$, the so-called Oseledec splitting: Naturally, they depend on the coordinates and the reference point \mathbf{u}_0 on the attractor, but like the corresponding exponents, they are also norm-independent [51]. How are the two Oseledec splittings at two different points on the same trajectory $\mathbf{u}(t_0 + t)$ linked to each other? A corollary of Eq. (2.54) is that

$$\lim_{t \rightarrow \infty} \frac{1}{t} \ln \left\| \mathbf{J}_{\Phi^t}^{\mathbf{u}_0} \delta \mathbf{u}_0 \right\| \leq \lambda^{(i)} \quad \Leftrightarrow \quad \delta \mathbf{u}_0 \in \mathfrak{E}_{\mathbf{u}_0}^{(i)}. \quad (2.63)$$

The suffix \mathbf{u}_0 was added to $\mathfrak{E}^{(i)}$ in order to indicate the reference point in phase space to which the Oseledec splitting is attached. The above question now reads: what can be said about $\mathfrak{E}_{\mathbf{u}_1}^{(i)}$ with $\mathbf{u}_1 = \mathbf{u}(t_0 + t_1)$? Similarly to Eq. (2.56), we have for $t > t_1$:

$$\mathbf{J}_{\Phi^t}^{\mathbf{u}_0} = \mathbf{J}_{\Phi^{t-t_1}}^{\mathbf{u}_1} \mathbf{J}_{\Phi^{t_1}}^{\mathbf{u}_0} \quad (2.64)$$

If we assume that $\mathbf{J}_{\Phi^{t_1}}^{\mathbf{u}_0}$ is invertible, then substituting Eq. (2.64) into Eq. (2.63) yields

$$\lim_{t \rightarrow \infty} \frac{1}{t} \ln \left\| \mathbf{J}_{\Phi^{t-t_1}}^{\mathbf{u}_1} \mathbf{J}_{\Phi^{t_1}}^{\mathbf{u}_0} \delta \mathbf{u}_0 \right\| \leq \lambda^{(i)} \quad \Leftrightarrow \quad \delta \mathbf{u}_0 \in \mathfrak{E}_{\mathbf{u}_0}^{(i)} \quad \xLeftrightarrow{\text{invertibility}} \quad \mathbf{J}_{\Phi^{t_1}}^{\mathbf{u}_0} \delta \mathbf{u}_0 \in \mathbf{J}_{\Phi^{t_1}}^{\mathbf{u}_0} \mathfrak{E}_{\mathbf{u}_0}^{(i)}. \quad (2.65)$$

As $\mathbf{J}_{\Phi^{t_1}}^{\mathbf{u}_0}$ is invertible, i.e. bijective, $\mathbf{J}_{\Phi^{t_1}}^{\mathbf{u}_0} \delta \mathbf{u}_0$ can be an arbitrary vector within $\mathbf{J}_{\Phi^{t_1}}^{\mathbf{u}_0} \mathfrak{E}_{\mathbf{u}_0}^{(i)}$. Defining $\delta \mathbf{u}_1 := \mathbf{J}_{\Phi^{t_1}}^{\mathbf{u}_0} \delta \mathbf{u}_0$, we thus have

$$\lim_{t \rightarrow \infty} \frac{1}{t} \ln \left\| \mathbf{J}_{\Phi^{t-t_1}}^{\mathbf{u}_1} \delta \mathbf{u}_1 \right\| \leq \lambda^{(i)} \quad \Leftrightarrow \quad \delta \mathbf{u}_1 \in \mathbf{J}_{\Phi^{t_1}}^{\mathbf{u}_0} \mathfrak{E}_{\mathbf{u}_0}^{(i)}, \quad (2.66)$$

i.e. $\mathbf{J}_{\Phi^{t_1}}^{\mathbf{u}_0} \mathfrak{E}_{\mathbf{u}_0}^{(i)}$ is actually $\mathfrak{E}_{\mathbf{u}_1}^{(i)}$. In general, the subspaces are thus *covariant* with the linearized dynamics [47]:

$$\mathfrak{E}_{\mathbf{u}(t_0+t)}^{(i)} = \mathbf{J}_{\Phi^t}^{\mathbf{u}_0} \mathfrak{E}_{\mathbf{u}_0}^{(i)} \quad (2.67)$$

2.1.8.3 Lyapunov Vectors

Assuming again invertibility of the linearized flow, everything said so far for $\mathbf{J}_{\Phi^t}^{\mathbf{u}_0}$ can likewise be defined for $\left(\mathbf{J}_{\Phi^t}^{\mathbf{u}(t_0-t)} \right)^{-1}$ which is the flow mapping a vector in tangent

space from time t_0 back to $t_0 - t$. If we use the notation $\neg X$ for the definition of any variable X corresponding to this inverted flow and number Lyapunov exponents and eigenspaces in reverse order, i.e. $\neg\lambda_i < \neg\lambda_j$ for $i < j$, Eq. (2.53) implies

$$\lambda_i = -\neg\lambda_i, \quad 1 \leq i \leq n, \quad (2.68)$$

as, due to Oseledec's theorem, the Lyapunov exponents do not depend on the starting point on the attractor, and the inverted matrix has reciprocal eigenvalues. Furthermore, we read off Eq. (2.54):

$$\neg\lambda^{(i)} = \lim_{t \rightarrow \infty} \frac{1}{t} \ln \left\| \left(J_{\Phi^t}^{\mathbf{u}(t_0-t)} \right)^{-1} \delta \mathbf{u}_0 \right\| \quad \delta \mathbf{u}_0 \in \neg\mathfrak{E}_{\mathbf{u}_0}^{(i)} \setminus \neg\mathfrak{E}_{\mathbf{u}_0}^{(i-1)} \subset \mathbb{R}^n \quad (2.69)$$

$\neg\mathfrak{E}_{\mathbf{u}_0}^{(i)}$ is the subspace of \mathbb{R}^n which is spanned by eigenspaces for which $\neg\lambda \leq \neg\lambda^{(i)}$:

$$\neg\mathfrak{E}_{\mathbf{u}_0}^{(i)} = \text{span}(\neg E_{\mathbf{u}_0}^{(1)}, \neg E_{\mathbf{u}_0}^{(2)}, \dots, \neg E_{\mathbf{u}_0}^{(i)})$$

and for consistency we define $\neg\mathfrak{E}_{\mathbf{u}_0}^{(0)} := \{0\}$. An intuitive interpretation of Eq. (2.69) is: if initialized sufficiently far in the past, perturbations growing like $-\lambda^{(i)} = \lambda^{(i)}$ (forward in time) will end up in $\neg\mathfrak{E}_{\mathbf{u}_0}^{(i)} \setminus \neg\mathfrak{E}_{\mathbf{u}_0}^{(i-1)}$ at t_0 . Equation (2.54) therefore describes the set of initial conditions which grow with a specific rate, whereas Eq. (2.69) determines the images of this set under the linearized flow. In analogy to Eq. (2.63), $\neg\mathfrak{E}_{\mathbf{u}_0}^{(i)}$ is the subspace of vectors that grow backward in time with a rate $\leq \neg\lambda^{(i)}$ or equivalently with a rate $\geq \lambda^{(i)}$ forward in time:

$$\lim_{t \rightarrow \infty} -\frac{1}{t} \ln \left\| \left(J_{\Phi^t}^{\mathbf{u}(t_0-t)} \right)^{-1} \delta \mathbf{u}_0 \right\| \geq \lambda^{(i)} \quad \Leftrightarrow \quad \delta \mathbf{u}_0 \in \neg\mathfrak{E}_{\mathbf{u}_0}^{(i)} \quad (2.70)$$

Like the $\mathfrak{E}_{\mathbf{u}_0}^{(i)}$, the $\neg\mathfrak{E}_{\mathbf{u}_0}^{(i)}$ are thus covariant. Since the eigenspaces $\neg E_{\mathbf{u}_0}^{(i)}$ are orthogonal, we can find an orthonormal basis $\neg \mathbf{e}_{\mathbf{u}_0}^i$, $1 \leq i \leq n$ of \mathbb{R}^n such that

$$\neg\mathfrak{E}_{\mathbf{u}_0}^{(i)} = \text{span}(\neg \mathbf{e}_{\mathbf{u}_0}^1, \neg \mathbf{e}_{\mathbf{u}_0}^2, \dots, \neg \mathbf{e}_{\mathbf{u}_0}^d), \quad d = \dim \neg\mathfrak{E}_{\mathbf{u}_0}^{(i)}, \quad 1 \leq i \leq \tilde{n}. \quad (2.71)$$

This basis is unique apart from the choice of an arbitrary orthonormal basis within the eigenspaces with $\dim \neg E_{\mathbf{u}_0}^{(i)} > 1$. If a basis fulfills this requirement, the vectors $\mathbf{e}_{\mathbf{u}_0}^i$ are termed *Backward Lyapunov vectors* [52], because they depend on the action of the flow in the past. Similarly, *Forward Lyapunov vectors* can be defined in the same way as an orthonormal basis of the covariant subspaces $\mathfrak{E}_{\mathbf{u}_0}^{(i)}$. Another name for the backward Lyapunov vectors is *Gram-Schmidt vectors* [52, 53], because they are linked to the matrices \mathbf{Q}^i defined above in the following way and the QR-decomposition can be obtained by *Gram-Schmidt orthogonalization*:

Assume $q = \dim \mathfrak{E}_{\mathbf{u}_0}^{(q^*)}$ for some fixed q^* . The first q columns of the matrix \mathbf{Q}^i constructed in Sect. 2.1.8 span a subspace contained in $J_{\Phi^i \Delta t}^{\mathbf{u}_0} \left(\mathfrak{E}_{\mathbf{u}_0}^{(1)} \setminus \mathfrak{E}_{\mathbf{u}_0}^{(q^*+1)} \right)$. According

to Eq. (2.54), $\mathfrak{E}_{\mathbf{u}_0}^{(1)} \setminus \mathfrak{E}_{\mathbf{u}_0}^{(q^*+1)} \subset \mathbb{R}^n$ contains all (and only those) vectors that asymptotically grow under the action of the linearized flow with exponential rates $\geq \lambda^{(q^*)} = \lambda_q$. Therefore, it follows from Eq. (2.70) that the subspace spanned by the first q columns of \mathbf{Q}^i tends towards ${}^{-}\mathfrak{E}_{\mathbf{u}(t_0+i\Delta t)}^{(i)}$ for large t (or i). Since the subspace is by construction q -dimensional, the first q columns of \mathbf{Q}^i thus tend to the backward Lyapunov vectors ${}^{-}\mathbf{e}_{\mathbf{u}(t_0+i\Delta t)}^1, {}^{-}\mathbf{e}_{\mathbf{u}(t_0+i\Delta t)}^2, \dots, {}^{-}\mathbf{e}_{\mathbf{u}(t_0+i\Delta t)}^q$. As mentioned above, once converged to the corresponding backward eigenspaces, they are unique except for the freedom of choosing arbitrary orthogonal vectors within the eigenspaces of dimensionality greater than 1. For those cases, the backward Lyapunov vectors one obtains depend on the initially chosen vectors spanning the q -dimensional subspace of $\mathfrak{E}_{\mathbf{u}_0}^{(1)} \setminus \mathfrak{E}_{\mathbf{u}_0}^{(q^*+1)}$.

The eigenspaces ${}^{-}E^{(i)}$ themselves are not covariant, because the ${}^{-}E^{(i)}$ are by construction orthogonal, but the linearized flow is not, in general, angle preserving. This implies that the Gram-Schmidt vectors are not covariant, either. Obviously, since orthogonality is defined via a norm, they are not norm-independent. However, there is a set of covariant, norm-independent vectors spanning the same covariant subspaces ${}^{-}\mathfrak{E}_{\mathbf{u}(t_0+i\Delta t)}^{(i)}$, which can be obtained from sets of forward and backward Lyapunov vectors [52–54]. Consequently they are known as *covariant Lyapunov vectors*. Despite their recent popularity [52, 53, 55–58], some authors noticed advantages of the Gram-Schmidt Lyapunov vectors, namely their directionality with respect to time [58]: by construction, they only depend on the past history of the trajectory (cf. Eq. (2.69)), making them a more “causal” object than the covariant Lyapunov vectors which are invariant under time reversal.

In Sect. 3.1, Lyapunov exponents and Gram-Schmidt vectors will be used to characterize activation patterns in excitable media. The numerical implementation for this specific type of system and its compatibility to the abstract dynamical system of Eq. (2.46) considered in this section will be outlined in Sect. 2.2.6.

2.2 Numerical Implementation

2.2.1 Time Stepping Scheme

Simulations of cardiac tissue using mathematical models as described in Sects. 2.1.3 and 2.1.6 require the numerical solution of PDEs or, more specifically, *reaction-diffusion equations* (RDEs). These are of the form of Eq. (2.13) (p. 33). All numerical results in this thesis are based on the numerical procedure of *finite differences*: Let

$$\frac{\partial u}{\partial t} = f(u, \mathbf{h}) + \mathcal{L}[u] \quad (2.72a)$$

$$\frac{\partial \mathbf{h}}{\partial t} = \mathbf{H}(u, \mathbf{h}) \quad (2.72b)$$

be the prototypical RDE that is to be solved. $u(\mathbf{x}, t)$ is the solution for the diffusing variable defined on some domain $\mathcal{D} \times [0, T[\subset \mathbb{R}^d \times \mathbb{R}$ with $d \in \{1, 2, 3\}$. $f : \mathbb{R}^n \rightarrow \mathbb{R}$ is the local reaction term and \mathcal{L} is the diffusion term (a linear operator) which acts spatially on u . \mathbf{h} denotes the vector of local variables and \mathbf{H} defines the corresponding dynamics, as in, e.g., Eq. (2.13). All simulations in this thesis are *initial value problems*, meaning that $u(\mathbf{x}, t = 0)$ and $\mathbf{h}(\mathbf{x}, t = 0)$ are given and the solution for $t \in]0, T[$ is to be determined. For this purpose, the solution (u, \mathbf{h}) is discretized spatially and temporally, with discretization steps h_x, h_y and h_z in the (at most) three space directions and Δt in time. This means that the solution is only known at spatially equidistant nodes. Rectangular computational spatial domains are used, even if the physical domain \mathcal{D} is not rectangular, using the phase-field method introduced in Sect. 2.1.5, whose numerical implementation will be explained in Sect. 2.2.3. If the computational domain has a length L_l in direction l ($l \in \{x, y, z\}$), the l -position of node number i is defined to be

$$\pi_l(i) = \frac{(1 + 2i)h_l - L_l}{2} \quad i \in \mathbb{N}^0, 0 \leq i \leq N_l - 1 \quad (2.73)$$

The convention $h_l = L_l/N_l$ is used, where N_l is the number of nodes in l -direction. In the case of three spatial dimensions, this implies that the computational domain is $] -L_x/2, L_x/2[\times] -L_y/2, L_y/2[\times] -L_z/2, L_z/2[\subset \mathbb{R}^3$ and that the nodes are placed at the centers of the computational voxels that are $h_x \times h_y \times h_z$ in size. An exemplary geometrical arrangement for a one-dimensional domain is shown in Fig. 2.9. Numerically, the solution u thus consists of a finite number of values referred to as $u_{i,j,k}^\tau$, where i, j and k denote the three spatial indices and τ the time index:

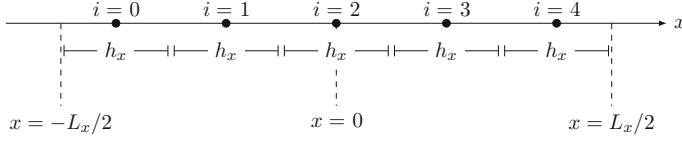


Fig. 2.9 Numerical grid points in a one-dimensional domain. The simulation domain is $\mathcal{D} =] -L_x/2, L_x/2[\subset \mathbb{R}$. $N_x = 5$ numerical nodes are used, whose positions $\pi_x(i)$ are indicated by black dots. Each node is centered in a computational box $h_x = L_x/N_x$ in size

$$u_{i,j,k}^\tau := u(\pi_x(i), \pi_y(j), \pi_z(k), \Delta t \cdot \tau) \quad (2.74)$$

$$\text{with } i \in \mathbb{N}^0, 0 \leq i \leq N_l - 1 \quad \forall l \in \{x, y, z\} \quad (2.75)$$

$$\text{and } \tau \in \mathbb{N}^0, 0 \leq \tau \leq \frac{T}{\Delta t} \quad (2.76)$$

The time stepping of consecutive values for all spatial nodes from the initial values $u_{i,j,k}^0$ is done using a simple *forward Euler* or *forward-time centered-space* (FTCS) scheme:

$$u_{i,j,k}^{\tau+1} = u_{i,j,k}^\tau + \Delta t \left(f(u_{i,j,k}^\tau) + (L[\mathbf{u}^\tau])_{i,j,k} \right) \quad (2.77)$$

Here, L refers to the approximation of the diffusion operator \mathcal{L} in Eq.(2.72). In contrast to \mathcal{L} , L acts on the discretized field \mathbf{u}^τ , where this vector quantity contains the set of u -values at all numerical grid points at the time step τ . L is usually expressed as a weighted sum of neighboring points, as will be discussed in detail in Sect. 2.2.2, so it acts like a (sparse) matrix on the vector \mathbf{u}^τ . $(L[\mathbf{u}^\tau])_{i,j,k}$ refers to the node (i, j, k) of the result of this operator approximation. The time stepping of the local variables (the components of \mathbf{h}) is done in the same way as in Eq.(2.77), only without the diffusion term.

2.2.2 Diffusion Term

Approximations of the linear operator \mathcal{L} can be obtained in different ways, depending on the specific form of \mathcal{L} . They all have in common that the approximation L can usually be written as a convolution of the form:

$$\begin{aligned} (\mathcal{L}[u]) (\pi_x(k^*), \pi_y(l^*), \pi_z(m^*)) &\approx (L[\mathbf{u}])_{k^*, l^*, m^*} \\ &= \sum_{k, l, m \in \{-1, 0, 1\}} \alpha_{k, l, m} \underbrace{u_{k^*+k, l^*+l, m^*+m}}_{=(T_m^z T_l^y T_k^x u)_{k^*, l^*, m^*}}. \end{aligned} \quad (2.78)$$

The time dependence has been omitted and will be for the rest of this section, as \mathcal{L} and L act solely on the spatial degrees of freedom. Defining a discrete approximation L for \mathcal{L} now reduces to finding a suitable kernel α . For this purpose, it is useful to define the translation operator $T_h^i u$, which takes the field u and shifts it by a given amount $-nh_i$ in the direction i , where $i \in x, y, z$, such that

$$(T_{+1}^x u)(x, y, z) = u(x + h_x, y, z) \quad (2.79)$$

$$\text{or} \quad (T_{+1}^x u)_{k,l,m} = u_{k+1,l,m}. \quad (2.80)$$

From the definition it follows that translation operators in the same direction follow the summation rule

$$T_{n_1}^i T_{n_2}^i u = T_{n_1+n_2}^i u \quad (2.81)$$

and that they correspond to the identity if the shift is zero, i.e.

$$T_0^i u = u. \quad (2.82)$$

In the following, $\delta_{i,j}$ denotes the Kronecker delta, which is 1 if and only if $i = j$ and 0 otherwise. The inverse Kronecker delta $\bar{\delta}$ is defined as $\bar{\delta}_{i,j} = 1 - \delta_{i,j}$.

2.2.2.1 General Diffusion Tensors

A discretization for the general form of the diffusion term $\mathcal{L} = \nabla \cdot \underline{D} \nabla$ with a space-dependent diffusion tensor \underline{D} can be obtained by approximating all derivatives by centered finite differences, i.e. $\partial_i u \approx (T_{\frac{1}{2}}^i u - T_{-\frac{1}{2}}^i u)/h_i$, where ∂_i is the spatial derivative in the direction i and h_i the corresponding spatial discretization step. In the most general case, \underline{D} is space-dependent, which means that each component D_{ij} of \underline{D} is itself a field. For values of u and D_{ij} in between two numerical grid points, the definition

$$T_{\frac{\mu}{2}}^i := \frac{T_0^i + T_{\mu}^i}{2} \quad (2.83)$$

is used, where $\mu \in \{1, -1\}$. In this way, the following expansion for a general diffusion term is obtained:

$$\begin{aligned}
\nabla \cdot \underline{D} \nabla u &= \sum_{i \in \{x, y, z\}} \partial_i \sum_{j \in \{x, y, z\}} D_{ij} \partial_j u \\
&\approx \sum_{i \in \{x, y, z\}} \frac{1}{h_i} \partial_i \left(\sum_{j \in \{x, y, z\}} D_{ij} (T_{\frac{1}{2}}^j u - T_{-\frac{1}{2}}^j u) \right) \\
&\approx \sum_{i=j} \frac{1}{h_i^2} (T_{\frac{1}{2}}^i D_{ii} \cdot (T_1^i u - u) - T_{-\frac{1}{2}}^i D_{ii} \cdot (u - T_{-1}^i u)) \\
&\quad + \sum_{i \neq j} \frac{1}{h_i h_j} \left[T_{\frac{1}{2}}^i D_{ij} \cdot (T_{\frac{1}{2}}^i T_{\frac{1}{2}}^j u - T_{\frac{1}{2}}^i T_{-\frac{1}{2}}^j u) \right. \\
&\quad \quad \left. - T_{-\frac{1}{2}}^i D_{ij} \cdot (T_{-\frac{1}{2}}^i T_{\frac{1}{2}}^j u - T_{-\frac{1}{2}}^i T_{-\frac{1}{2}}^j u) \right] \\
&= \sum_{i=j} \frac{1}{h_i^2} \sum_{\mu \in \{-1, 1\}} T_{\frac{\mu}{2}}^i D_{ii} \cdot (T_{\mu}^i u - u) \\
&\quad + \sum_{i \neq j} \frac{1}{4 h_i h_j} \left[T_{\frac{1}{2}}^i D_{ij} \cdot (T_1^i T_1^j u + T_1^j u - T_1^i T_{-1}^j u - T_{-1}^j u) \right. \\
&\quad \quad \left. - T_{-\frac{1}{2}}^i D_{ij} \cdot (T_{-1}^i T_1^j u + T_1^j u - T_{-1}^i T_{-1}^j u - T_{-1}^j u) \right] \\
&= \sum_{i=j} \frac{1}{h_i^2} \sum_{\lambda \in \{-1, 1\}} \sum_{\mu \in \{-1, 1\}} \lambda \mu T_{\frac{\mu}{2}}^i D_{ii} \cdot (\delta_{\mu, \lambda} T_{\mu}^i u + \bar{\delta}_{\mu, \lambda} u) \\
&\quad + \sum_{i \neq j} \frac{1}{4 h_i h_j} \sum_{\lambda \in \{-1, 1\}} \sum_{\mu \in \{-1, 1\}} \lambda \mu T_{\frac{\mu}{2}}^i D_{ij} \cdot (T_{\mu}^i T_{\lambda}^j u + T_{\lambda}^j u) \\
&= \sum_{\substack{i, j \in \{x, y, z\} \\ \lambda, \mu \in \{-1, 1\}}} \frac{\lambda \mu T_{\frac{\mu}{2}}^i D_{ij}}{h_i h_j} \cdot \left[\delta_{i, j} \left(\delta_{\mu, \lambda} T_{\mu}^i u + \bar{\delta}_{\mu, \lambda} u \right) \right. \\
&\quad \quad \left. + \frac{\bar{\delta}_{i, j}}{4} \left(T_{\mu}^i T_{\lambda}^j u + T_{\lambda}^j u \right) \right] \tag{2.84}
\end{aligned}$$

At most two shift operators are applied to u in Eq. (2.84), such that by comparison with (2.78), $\alpha_{k, l, m} = 0$ for $|k| = |l| = |m| = 1$. The remaining elements of the kernel $\alpha_{k, l, m}$ can be calculated directly by iterating through the kernel as suggested by Eq. (2.84) (see Listing 2.1).

Listing 2.1: Calculation of Laplace kernel for a space dependent diffusion tensor. The kernel elements $\alpha_{k,l,m}$ are constructed for one specific point in the computational domain and saved to the array *kernel*. The scheme follows exactly equation (2.84), see also comments in the code.

```

1 void PhaseFieldAddPotentialUpdater::buildKernel(const Array<double>&
... sigma_halves, Array<double>& kernel) const {
2     kernel.setTo(0);
3     // position in kernel
4     vector<std::size_t> inKernel;
5     for(unsigned int dir = 1; dir<=3; dir++) {
6         for(unsigned int odir = 1; odir <=3; odir++) {
7             if(laplaceDirections(dir) && laplaceDirections(odir)) {
8                 for(int pm=-1; pm<=1; pm+=2) {
9                     for(int pm2=-1; pm2<=1; pm2+=2) {
10                        /* sigma_halves(i,j,k,(pm+1)/2+1) contains diffusion tensor
11                        component  $D_{ij}$  for the current position shifted by pm/2
12                        in direction k.*/
13                            double factor = 1./((gridStep(dir)*gridStep(odir))*
... pm*pm2*sigma_halves(dir,odir,dir,(pm+1)/2+1)
... ;
14                            if(pm==pm2 && dir==odir) {
15                                // zero = center point
16                                    inKernel=zero;
17                                    kernel(inKernel) += factor;
18                                }
19                                if(pm==pm2 && dir==odir) {
20                                    inKernel=zero;
21                                // operator [] is zero based, thus dir-1
22                                    inKernel[dir-1]=(int)inKernel[dir-1]+pm;
23                                    kernel(inKernel) += factor;
24                                }
25                                if(dir!=odir) {
26                                    inKernel=zero;
27                                    inKernel[odir-1]=(int)inKernel[odir-1]+pm2;
28                                    kernel(inKernel) += factor/4.;
29
30                                    inKernel=zero;
31                                    inKernel[dir-1]=(int)inKernel[dir-1]+pm;
32                                    inKernel[odir-1]=(int)inKernel[odir-1]+pm2;
33                                    kernel(inKernel) += factor/4.;
34                                }
35                            }
36                        }
37                    }
38                }
39            }
40 }

```

2.2.2.2 Homogeneous, Isotropic Diffusion

For spatially constant and isotropic diffusion tensors $\underline{D} = D\text{Id}$, i.e. $\mathcal{L} = \nabla \cdot \underline{D} \nabla = D\nabla^2$, throughout the computational domain, and equal discretization steps $h_x = h_y = h_z = h$ in all directions, the kernel elements $\alpha_{k,l,m}$ become symmetric in the sense that

$$|k_1| + |l_1| + |m_1| = |k_2| + |l_2| + |m_2| \Rightarrow \alpha_{k_1,l_1,m_1} = \alpha_{k_2,l_2,m_2}, \quad (2.85)$$

meaning that only the number of non-zero indices k, l, m determines the value of the kernel element. From Eq. (2.84), the following values are obtained:

$$\alpha_{k,l,m} = \frac{D}{h^2} \cdot \begin{cases} -6 & \text{for } k = l = m = 0 \\ 1 & \text{for } |k| + |l| + |m| = 1 \\ 0 & \text{for } |k| + |l| + |m| = 2 \end{cases} \quad (2.86)$$

Under the assumption $\mathbf{T}_1^z u = \mathbf{T}_{-1}^z u = u$, all derivatives in the z -direction vanish and the dynamics for a two-dimensional medium is obtained. Thus, a two-dimensional kernel $\alpha_{k,l}^{2d}$ can be obtained by setting $\alpha_{k,l}^{2d} = \sum_{m=-1,0,1} \alpha_{k,l,m}$ for all k, l . In this case, the kernel reduces to the usual *five-point stencil* (see Eq. 12.5.1 in Ref. [59]) for the Laplacian $D\nabla^2$:

$$\left(\alpha_{k,l}^{2d} \right)_{\substack{k=-1,0,1 \\ l=-1,0,1}} = \frac{D}{h^2} \begin{pmatrix} 0 & 1 & 0 \\ 1 & -4 & 1 \\ 0 & 1 & 0 \end{pmatrix}. \quad (2.87)$$

A Taylor expansion of $u(x, y)$ reveals that the approximation $\alpha^{2d}L$ for the Laplacian defined by this kernel (and also by the $\alpha_{k,l,m}$ above) is second order accurate, i.e. $\nabla^2 u = \alpha^{2d}Lu + \mathcal{O}(h^2)$, which is to be expected because it originates from the second-order finite difference discretization in Sect. 2.2.2.

If isotropy and a spatially constant diffusion tensor \underline{D} are present, instead of α above, the following kernel $\tilde{\alpha}$ can be used:

$$\tilde{\alpha}_{k,l,m} = \frac{D}{30h^2} \cdot \begin{cases} -128 & \text{for } k = l = m = 0 \\ 14 & \text{for } |k| + |l| + |m| = 1 \\ 3 & \text{for } |k| + |l| + |m| = 2 \\ 1 & \text{for } |k| + |l| + |m| = 3 \end{cases} \quad (2.88)$$

Again, it is defined for $-1 \leq k, l, m \leq 1$. A Taylor expansion shows that this kernel is second-order accurate and thus might not seem to have any advantage over α . However, it preserves the rotational symmetry of the Laplacian much more accurately, which results in reduced grid-induced distortions of the dynamics at a fixed spatial

discretization length h . Using the same method as above, the two-dimensional version of this stencil can be calculated as

$$\left(\tilde{\alpha}_{k,l}^{2d}\right)_{\substack{k=-1,0,1 \\ l=-1,0,1}} = \frac{D}{6h^2} \begin{pmatrix} 1 & 4 & 1 \\ 4 & -20 & 4 \\ 1 & 4 & 1 \end{pmatrix}, \quad (2.89)$$

the so-called *nine-point stencil* (see Eq. 12.5.4 in Ref. [59]).⁹

2.2.3 Boundary Conditions

2.2.3.1 Rectangular Domains

For numerical grid points on the boundary, the convolution (2.78) contains neighbor points outside the actual computational domain, whose values are not defined. When \underline{D} is spatially constant and isotropic, these can be used to implement the desired boundary condition in conjunction with the simple kernels introduced in Sect. 2.2.2: For a rectangular grid, the normal fluxes $\mathbf{n} \cdot \underline{D} \nabla u$ at the boundaries are just derivatives of u along grid directions. For example, the flux at the boundary $x = \pi_x(0)$ can be approximated by a simple centered finite difference:

$$\mathbf{n} \cdot \underline{D} \nabla u \Big|_{x=\pi_x(0)} = D_{1,1} \frac{\partial u}{\partial x} \Big|_{x=\pi_x(0)} \approx D_{1,1} \frac{u_{1,j,k} - u_{-1,j,k}}{2h_x} \quad (2.90)$$

For no-flux boundary conditions, this term has to vanish, so defining $u_{-1,j,k} := u_{1,j,k}$ yields the desired result. For *periodic boundary conditions*, the numerical point just outside the domain is actually identical to the one on the opposing side. Therefore the definition in this case reads $u_{-1,j,k} := u_{N_x-1,j,k}$. The same method is applied to the boundary at $x = \pi_x(N_x - 1)$ and for the other space directions.

2.2.3.2 Domains of Arbitrary Shape

If \mathcal{D} is non-rectangular, the phase-field method introduced in Sect. 2.1.5 is employed. A large enough computational domain \mathcal{D}_c is chosen that contains \mathcal{D} . Then, for no-flux, technically, the replacement (2.19) is carried out by letting

$$\underline{D} = \phi \underline{D}_{\text{phys}}, \quad (2.91)$$

where $\underline{D}_{\text{phys}}$ is the physical diffusion tensor and ϕ is the phase field introduced in Sect. 2.1.5, describing the shape of the tissue domain \mathcal{D} . Even if $\underline{D}_{\text{phys}}$ is spatially

⁹ The fourth-order accuracy of the nine-point stencil sometimes referred to is only present under special circumstances (for example, for the solution of the Poisson equation), because the fourth-order error has a special form that can be corrected for in those cases.

constant, a space dependence of \underline{D} is introduced by the phase field. Thus, the numerical scheme developed in Sect. 2.2.2 is applied. After calculating the local kernel elements $\alpha_{k,l,m}$ according to Eq. (2.84), all weights have to be divided by the local value of the phase field $\phi(x)$ in order to account for the additional factor $1/\phi$ in Eq. (2.19). Since ϕ and $\underline{D}_{\text{phys}}$ are independent of time, this kernel calculation has to be carried out only once at the beginning of the simulation, allowing for an efficient implementation of no-flux boundary conditions for arbitrarily shaped tissue domains \mathcal{D} .

To enforce the more general boundary condition of the type of Eq. (2.36), the phase-field replacement (2.37) is rewritten as

$$\begin{aligned} \frac{1}{\phi} \nabla \cdot (\phi(\underline{D} \nabla u - \mathbf{E})) &= \frac{1}{\phi} \nabla \cdot (\phi \underline{D} \nabla u + \tilde{\underline{D}} \nabla v_E) \\ &= \frac{1}{\phi} \nabla \cdot (\phi \underline{D} \nabla u) + \frac{1}{\phi} \nabla \cdot (\phi \tilde{\underline{D}} \nabla v_E) \end{aligned} \quad (2.92)$$

where v_E is chosen such that $\mathbf{E} = -\tilde{\underline{D}} \nabla v_E$. If the outside potential v_o in Eq. (2.16) (p. 32) is assumed to have a constant gradient, v_E is identical to v_o , with an appropriately chosen $\tilde{\underline{D}}$. Substituting the right hand side of Eq. (2.92) for $\mathcal{L}[u]$ in Eq. (2.72a), the numerical scheme introduced in Sect. 2.2.2 can be applied to both diffusion terms, as explained above for the no-flux case. Splitting up the two terms as in Eq. (2.92) is particularly convenient, if the assumed potential v_E is independent of time or merely multiplied by a time-dependent prefactor. In this case, the entire second term has to be calculated only once at the beginning of the simulation. The result of this calculation (a field of the size of the computational domain \mathcal{D}_c) is then multiplied by Δt and possibly the time-dependent factor, before being added to Eq. (2.77).

As mentioned in [26], the results of a numerical simulation with the phase-field method change only insignificantly if numerical calculations are performed solely for grid points for which $\phi_{i,j,k} > \phi_{\text{cut-off}}$ with $\phi_{\text{cut-off}} \ll 1$. The spatial domain in which $\phi > \phi_{\text{cut-off}}$ holds corresponds to a slightly enlarged tissue domain \mathcal{D} within the auxiliary domain \mathcal{D}_c . As explained in Sect. 2.1.5, the pseudo-advection term in the phase-field method leads to a relative independence of the dynamics in \mathcal{D} from the boundary condition imposed at $\partial \mathcal{D}_c$. In essence, skipping the numerical update step for the values of computational points for which $\phi_{i,j,k} < \phi_{\text{cut-off}}$ corresponds to an artificial Dirichlet boundary condition imposed at the boundary of the enlarged tissue domain (which would also be a valid choice for \mathcal{D}_c , but usually rectangular domains are used). Therefore, the validity of this approach follows from the line of thoughts in Sect. 2.1.5. In all simulations throughout this thesis $\phi_{\text{cut-off}} = 10^{-5}$ is used.

2.2.4 Stability Considerations

For the assessment of numerical stability, the nature of the different terms of the RDE has to be taken into account. One limitation arises from the typically large upstroke

velocity of the membrane potential for a beginning excitation in cardiac models, which is a result of the local reaction term f in Eq. (2.72) or correspondingly $-I_{\text{ion}}/C_m$ in Eq. (2.13). A name often used to describe problems with strongly differing time scales is *stiff systems*. To avoid instabilities due to this stiffness, the time step for an explicit Euler scheme like Eq. (2.77) has to be considerably smaller than the time scale $\tau_{\text{upstroke}} = A_{\text{AP}}/v_{\text{upstroke}}$, where A_{AP} is the action potential amplitude and v_{upstroke} is the maximal rate of change during the upstroke. As the typical upstroke time in cardiac cells is on the millisecond order, this restricts Δt to the sub-millisecond range for models that work with real units.

Another possible instability arises from the diffusion term. If Eq. (2.77) is considered without the reaction term, for isotropic diffusion $\underline{D} = D\text{Id}$, the discretized version of a heat equation is obtained. Applying a *von Neumann stability analysis* to this discretization (using the kernels of Eq. (2.86)) leads to a stability condition for the forward Euler scheme, namely

$$D \frac{\Delta t}{h^2} \leq \frac{1}{2d}, \quad (2.93)$$

where d is the number of spatial dimensions (Eq. 19.2.6 in Ref. [60] generalized to higher dimensions). This is a stringent restriction, since it means that a small h which might be necessary by itself to resolve spatial details of the dynamics automatically requires a quadratically smaller Δt . In three dimensions, if the left hand side of Eq. (2.93) is kept constant, halving h thus leads to an approximately 32-fold increase in computational cost, because the number of numerical grid points increases by a factor of eight and Δt has to be divided by four.

Both kinds of stability criteria could be relaxed or avoided by using more sophisticated time stepping schemes than FTCS. However, despite providing the desired stability, the additional computational cost—arising, e.g., for implicit methods from solving large systems of linear equations—does not necessarily bring about an equal increase in accuracy. The accurate numerical computation of the solution even on small spatial scales is desirable in particular for models of cardiac tissue, because the interaction of diffusion and rapid upstrokes on these scales is essential for the propagation of wave fronts. Thus, reducing h without reducing Δt to faithfully model the physics of the additional small scales is usually leading nowhere, even if stability is guaranteed by the numerical method. Nevertheless, computation time and memory consumption can be reduced to some extent by using alternative numerical schemes [61] (see [25] for a recent summary of widely-used techniques). However, considering the additional implementation and debugging costs in addition to the arguments above, an explicit FTCS scheme is a less unfavorable numerical scheme for this type of problem than it may seem at first sight.

It should be noted that the stability criterion (2.93) applies also to spatially varying diffusion tensors \underline{D} , as long as they vary slowly. In this case, the von Neumann stability analysis is thought to be carried out locally. This condition is certainly not fulfilled, when the phase-field method introduced in Sect. 2.1.5 is employed. Here, the diffusion tensor is multiplied by ϕ , a quantity which decays rapidly at the physical

system boundary. Far away from the physical domain, it decays exponentially with a decay length $\approx \xi$ comparable to the grid spacing h . The normal derivative of the phase field is therefore $|d \ln \phi / dn| \lesssim 1/\xi$. According to Eq. (2.29), this leads to an advection-like term with a velocity of $|v| \lesssim D/\xi$, if the original diffusion tensor is again assumed to be isotropic with $\underline{D} = D \text{Id}$. For any explicit time stepping scheme of an advection equation, the *Courant-Friedrichs-Lewy criterion* for numerical stability applies (Eq. 19.1.17 in Ref. [60]):

$$1 \geq \frac{|v|\Delta t}{h} \gtrsim D \frac{\Delta t}{\xi h} \quad (2.94)$$

The values for ξ used in this thesis range between $h/2$ and h such that Eq. (2.94) is not a more stringent restriction on Δt than Eq. (2.93). Of course, this calculation is only an approximation and Eq. (2.94) should be taken as an order-of-magnitude estimation. Also, additional instabilities could arise from the steep increase of the advection velocity near the boundary of the physical domain, and the behavior at some intermediate distance from the boundary might also differ from the simple exponential decay due to the geometry of the boundary. However, Eq. (2.94) shows that, at zeroth order, there is no reason why the phase-field method should destabilize the numerical solution. In reality, test simulations show that numerical simulations using the phase-field method are mostly stable provided they were without the phase field ($\phi = 1$ everywhere). Only sometimes, it is necessary to reduce Δt slightly, never leaving, however, the order of magnitude suggested by Eq. (2.93).

2.2.5 Spiral Tip Detection

The tips of spiral waves in two-dimensional simulations of the Barkley model are localized by determining the topological charge of small test domains within the simulation domain according to Eq. (2.45). To numerically calculate the integral along a closed curve, the method of Iyer and Gray [41] is used:

$$2\pi n_{i,j}^{\text{top}} = \oint_{\mathcal{C}_{i,j}} \nabla \theta \, d\mathbf{l} \approx \sum_{m=2}^n \text{diff}(\theta_{i+k_m, j+l_m}, \theta_{i+k_{m-1}, j+l_{m-1}}) \quad (2.95)$$

The offsets k_1, \dots, k_n and l_1, \dots, l_n parameterize a path $\mathcal{C}_{i,j}$ around the point (i, j) in numerical coordinates. The function diff yields the phase difference between two points. As explained in Sect. 2.1.7, for the local phase differences, the branch of the arctan2 function has to be chosen such that there is no phase jump between the two points whose phase difference is to be determined. A unique difference is obtained by assuming that the phase difference is always smaller in magnitude than π :

$$\text{diff}(x, y) := \text{mod}(x - y + \pi, 2\pi) - \pi \in [-\pi, \pi[\quad (2.96)$$

The mod function is defined such that it returns positive values and thus the result of diff ends up in the desired range. As in Ref. [41], an eight-point integration path is chosen:

$$\begin{pmatrix} k_1, \dots, k_n \\ l_1, \dots, l_n \end{pmatrix} = \begin{pmatrix} 1 & 1 & 0 & -1 & -1 & -1 & 0 & 1 & 1 \\ 0 & 1 & 1 & 1 & 0 & -1 & -1 & -1 & 0 \end{pmatrix} \quad (2.97)$$

On the one hand, this integration path is small enough to minimize the risk of enclosing multiple phase singularities, such that isolated phase singularities can be detected. On the other hand, it contains enough sampling points to avoid large phase jumps on the integration path (after all, the phase differences have to add up to 2π if a phase singularity is enclosed). Such large jumps of θ could cause the definition Eq. (2.96) to miss full turns of the phase. Phase singularities and their corresponding spiral tips can then be detected by locating the points (i, j) for which $n_{i,j}^{\text{top}} = \pm 1$ in Eq. (2.95). Usually, four adjacent numerical points (a $2h \times 2h$ region) are detected as possible candidates for the location of a phase singularity, since the integration path encloses a region which is $2h \times 2h$ in size. Within this thesis, the position of the phase singularity is then defined to be in the center of this $2h \times 2h$ region.

2.2.6 Lyapunov Exponents and Vectors

2.2.6.1 Linearization of an Extended System

In Sect. 2.1.8, the theory of Lyapunov stability analysis and the standard mathematical strategy for its implementation were summarized for a general dynamical system like Eq. (2.46). In this thesis, the analysis is applied to extended systems of the type of Eq. (2.72). Obviously, in the framework of Sect. 2.1.8, it is not possible to include differential operators directly on the right hand side of Eq. (2.46). However, this is possible for the semi-discretized form of Eq. (2.72)

$$\begin{aligned} \frac{du_{i,j,k}}{dt} &= f(u_{i,j,k}, h_{1i,j,k}, h_{2i,j,k}, \dots) + (L[\mathbf{u}])_{i,j,k} \\ \frac{dh_{1i,j,k}}{dt} &= H_1(u_{i,j,k}, h_{1i,j,k}, h_{2i,j,k}, \dots) \\ \frac{dh_{2i,j,k}}{dt} &= H_2(u_{i,j,k}, h_{1i,j,k}, h_{2i,j,k}, \dots) \\ &\vdots \end{aligned} \quad \forall i, j, k \quad (2.98)$$

where the vector quantity \mathbf{u} again contains the values of u at all numerical nodes by defining a fixed mapping of (i, j, k) to a linear index. Similar vectors with the same mapping can be defined for each of the local variables h_i , which were summarized as $\mathbf{h} = (h_1, h_2, \dots)$ in, e.g., Eq. (2.4). For clarity, they have been separated here. As the approximation L for the differential operator \mathcal{L} is expressed as a convolution of the form (2.78), Eq. (2.98) represents a system of coupled ODEs, together with

the boundary conditions introduced in Sect. 2.2.3. Let the set of $u_{i,j,k}(t)$, $h_{1i,j,k}(t)$, $h_{2i,j,k}(t)$, ... for all i, j, k be a solution of this dynamical system. Then, the linearized dynamics of Eq. (2.49) (again, with all vector components given separately) has the following structure:

$$\begin{aligned}
 \frac{d\delta u_{i,j,k}}{dt} &= \mathbf{J}_f^{(u_{i,j,k}, h_{1i,j,k}, h_{2i,j,k}, \dots)} \delta u_{i,j,k} + (L[\delta \mathbf{u}])_{i,j,k} \\
 \frac{d\delta h_{1i,j,k}}{dt} &= \mathbf{J}_{H_1}^{(u_{i,j,k}, h_{1i,j,k}, h_{2i,j,k}, \dots)} \delta h_{1i,j,k} \\
 \frac{d\delta h_{2i,j,k}}{dt} &= \mathbf{J}_{H_2}^{(u_{i,j,k}, h_{1i,j,k}, h_{2i,j,k}, \dots)} \delta h_{2i,j,k} \\
 &\vdots
 \end{aligned} \quad \forall i, j, k \quad (2.99)$$

It is worth noting that the Jacobian matrices for f, H_1, H_2, \dots are indeed only the low-dimensional matrices for the local dynamics. Just like the functions f, H_1, H_2, \dots , they are identical for all numerical grid points of the discretization. For the models used in this thesis, they are easily calculated by hand for arbitrary values of u, h_1, h_2, \dots and can be found in Appendix A. To guarantee differentiability, the smooth Fenton-Karma model introduced in Sect. 2.1.6 is used instead of the original model. The discretization L of the operator \mathcal{L} introducing the spatial coupling is linear (as is the original operator). Thus, its Jacobian is the operator itself and its numerical implementation can be used without modification for the evolution of the linearized system.

For periodic or no-flux boundary conditions, this is true even at the boundary: According to the explanations in Sect. 2.2.3, both types of boundary conditions can be implemented by exchanging certain numerical points in the convolution (2.78) for others. This procedure preserves the linearity of the operator (in its discretized form), which is why the linearized operator again is just the operator itself. In fact, this strategy should work just as well for no-flux boundary conditions implemented by the phase field method, although, in this thesis, Lyapunov stability analysis will only be carried out for simple, rectangular geometries. For *Dirichlet boundary conditions* (not used in this thesis), a similar argument leads to the conclusion that the original boundary condition has to be replaced by a Dirichlet boundary condition with the value 0 everywhere on the boundary for the linearized operator.

A different way of looking at Eq. (2.99) is to view it as a discretization of the system of partial differential equations

$$\begin{aligned}
 \frac{\partial \delta u}{\partial t} &= \mathbf{J}_f^{(u, h_1, h_2, \dots)} \delta u + \mathcal{L}[\delta u] \\
 \frac{\partial \delta h_1}{\partial t} &= \mathbf{J}_{H_1}^{(u, h_1, h_2, \dots)} \delta h_1 \\
 \frac{\partial \delta h_2}{\partial t} &= \mathbf{J}_{H_2}^{(u, h_1, h_2, \dots)} \delta h_2 \\
 &\vdots
 \end{aligned} \quad (2.100)$$

where δu , δh_1 , δh_2 , ... are now functions of space again. In Ref. [51], Eckmann and Ruelle note that Lyapunov stability analysis is possible on function spaces. This is a first indication that the Lyapunov spectra obtained from the linearization of the semi-discretized system Eq. (2.98) might actually be used to characterize the original reaction-diffusion system itself. This will be investigated in detail in Sect. 3.1.

2.2.6.2 Orthonormalization

Most of the stability analysis will be carried out for two-dimensional systems. Assuming a spatial discretization with $N_x N_y$ nodes (according to the scheme introduced in Sect. 2.2.1) and a model with one diffusing variable and $N_v - 1$ local variables, the total number of degrees of freedom of the semi-discretized system (2.98) as well as for the linearized system (2.99) is $N_{\text{dof}} = N_x N_y N_v$. Typical numbers are $N_x = N_y = 150$ and, e.g. for the Barkley model, $N_v = 2$, resulting in $N_{\text{dof}} = 45,000$. To calculate the N_{lyap} leading Lyapunov exponents, N_{lyap} copies of the system (2.99) have to be integrated alongside the actual dynamics. Hence, the matrix \mathbf{A} from Sect. 2.1.8 containing one perturbation in each column is a $N_{\text{dof}} \times N_{\text{lyap}}$ -matrix. The perturbations are initialized randomly and orthonormalized at regular intervals. According to Sect. 2.1.8, they converge to the N_{lyap} backward Lyapunov vectors corresponding to the N_{lyap} most expanding directions. The accuracy of the Lyapunov exponents calculated as in Eq. (2.62) (p. 54) can be improved by averaging the growth rates only after this alignment of the perturbations has taken place. The amount of time the perturbations were allowed to align for will be indicated along with the results of the simulations in Sect. 3.1.

Because of the large number of rows, the Gram-Schmidt orthogonalization procedure used to compute the QR-decomposition of \mathbf{A} can be parallelized efficiently. The scalar products of different columns \mathbf{A} with the columns of \mathbf{Q} that have already been obtained are calculated in separate threads. Moreover, when the results of this calculation are used to subtract the projections of the preceding columns from the current column, work in different blocks of rows is separated between threads.

In addition, the orthonormalization interval Δt in Sect. 2.1.8.1 does not necessarily have to equal the numerical time step Δt in Sect. 2.2.1. In fact, the orthonormalization interval is the result of an arbitrary splitting of the linearized flow as Eqs. (2.56) and (2.58) indicate. The purpose of this splitting is to prevent the volume spanned by the perturbations from collapsing, which may happen if two of the perturbations become linearly dependent due to finite-precision arithmetics. Choosing a larger orthonormalization interval leads to a considerable gain in computation time, since the costly QR-decomposition has to be carried out less often. To check the validity of the results, the resulting Lyapunov exponents are compared with those from simulations for which the orthonormalization procedure was carried out in each time step. For all results presented in this thesis, the results were ensured to be numerically indistinguishable with regard to the criterion explained below.

2.2.6.3 Convergence Measure

The result of the Lyapunov stability analysis are the time-independent Lyapunov exponents $\lambda_1, \lambda_2, \dots, \lambda_{N_{\text{lyap}}}$ and the Gram-Schmidt vectors at different time points. The vectors correspond to the columns of \mathbf{Q} , each of which in turn consists of all the degrees of freedom of Eq. (2.99). According to Eq. (2.62), the Lyapunov exponents are time-averaged growth factors of the perturbations. Due to Oseledec's theorem [45], it is known that this average will converge to a well-defined Lyapunov exponent when $t \rightarrow \infty$. However, the time scales on which this happens depend strongly on the attractor the system is evolving on. Heuristically speaking, the system has to sample the attractor densely enough and must have acquired the typical probability of being found in a certain position on the attractor. To recover the Floquet exponents as Lyapunov exponents for a periodic system, either one well-converged trajectory of exactly one period in time has to be averaged, or the averaging time has to be much larger than the periodicity of the system.

In order to obtain a quantitative measure for the accuracy of the obtained Lyapunov exponents, the sum of Eq. (2.62) is split up to define partial averages of the growth rates as

$$\lambda_i^{(k)} = \frac{K}{m\Delta t} \sum_{l=(k-1)\frac{m}{K}+1}^{k\frac{m}{K}} \ln R_{ii}^l \quad \forall k : 1 \leq k \leq K, \quad (2.101)$$

where m as in Sect. 2.1.8 denotes the total number of orthonormalization steps and i is the index of the Lyapunov exponent counting from the largest one. The new parameter K defines the number of partial exponents that are calculated as if the averaging time had been only one K th of its actual value. The reasoning behind this is that the partial exponents will start to deviate from their average (which is just the overall estimated Lyapunov exponent), when the averaging time becomes too short. In contrast, in the limit $m \rightarrow \infty$, i.e. infinite simulation and averaging time, all of the partial exponents $\lambda_i^{(k)}$, $k = 1, \dots, K$ converge to the same value, the true Lyapunov exponent λ_i . The standard deviation across the set of partial exponents is taken as an accuracy measure for each calculated Lyapunov exponent λ_i . In order to avoid an accidental match of the averaging time for the partial Lyapunov exponents with a periodicity of the system, the above accuracy estimation is carried out for values of K from 2 to 10. The maximum of all the standard deviations calculated for different K then serves as an error measure for each Lyapunov exponent. These error measures will be plotted as error bars in Sect. 3.1 when appropriate.

2.2.7 Hardware, Software, Parallelization

All numerical simulations for this thesis were carried out on computer clusters of the Max Planck Institute for Dynamics and Self-Organization in Göttingen. Most of the calculations were done on the 16 machines of the Biomedical Physics Group with

8 cores each (two quad-core Intel® Xeon® X5355 CPUs @2.66 GHz) and 32GB of RAM. For some of the simulations, it was possible to use parts of the computer cluster of the Laboratory for Fluid Dynamics, Pattern Formation and Biocomplexity (LFPB), consisting of a total of 72 machines with 12 cores each (two hexa-core Intel® Xeon® X5650 CPUs @2.67 GHz) and 24GB of RAM.

All computers run a homogeneous Linux environment. The software *MediaSim* for carrying out the actual calculations is a modular framework for the simulation of extended systems and was completely self-written in C++. Its capabilities exceed those described in this numerical methods section (see Appendix C). In the course of the work for this thesis, it has become one of the standard numerical tools in the Biomedical Physics Group and was used and considerably consolidated and extended by several people, first of all D. Hornung [62]. A. Behrend and P. Linke used it for their Diploma thesis and Bachelor's thesis, respectively [63, 64]. Furthermore, A. Mayer extended the framework during the work for his Bachelor's thesis [65], as did H. tom Würden [66] in addition to his work as a student research assistant.

Many of the theoretical problems that are addressed in this work using numerical simulations (in particular in Sects. 3.1 and 3.2) require parameter scans, resulting in a large number of similar numerical simulations. The simplest form of parallelization therefore is to use the hundreds of cores available on the computer cluster to start N of these simulations in parallel. This results in a guaranteed reduction of the computation time to $1/N$ times the time required for sequential calculation on a single core (apart from marginal losses due to bandwidth limitation during file reading and writing operations). The same kind of trivial parallelization was applied to the analysis of experimental data for Sect. 3.3, which was implemented in MATLAB® [67].

If the number of available cores exceeds a small number of computationally intensive numerical simulations which have to be carried out at the same time, the numerical work can be split between different threads, thus using multiple or all cores on a single machine. For the models used in this thesis, the critical order of magnitude, for which a single-core calculation become too time-consuming, is typically reached for long-term, two-dimensional simulations at high spatial resolutions or three-dimensional simulations. In these cases, the computational domain is subdivided into strips of equal width. Each thread then carries out the calculations for all computational points in one strip. This parallelization technique is implemented in the framework *MediaSim* on the level of array operations and is therefore available to all higher-level algorithms. For the calculation of Lyapunov exponents and vectors, not only the QR-decomposition is parallelized (as described in Sect. 2.2.6), but also the time stepping in tangent space, where different perturbations are propagated in different threads. The threading strategy could in general be extended to computations distributed across different machines, e.g., via *Message-passing interface* libraries, but this has not been necessary so far.

2.3 Experimental Methods

A global measure for the electrical activity of the heart¹⁰ can be obtained via an ECG. Intracellular or surface electrodes can provide local information on the membrane potential of single cells or small tissue regions. However, for a detailed investigation of activation patterns in the heart, information with high spatial and temporal resolution on the excitatory state of the tissue is required. This has become possible through the use of so-called *Voltage-sensitive dye* or *potentiometric dyes*. These are fluorescent molecules which embed into the cell membrane and whose spectral properties depend on the membrane voltage through field-induced charge shift. They were discovered at the end of the 1960s in studies investigating general optical properties of nerve fibers and their changes due to propagating action potentials [68–70]. Soon after this proof-of-principle in nerve fibers was accomplished, the cardiac community recognized the chances and opportunities of this new technique [71, 72]. After the discovery and characterization of the potentiometric probe di-4-ANEPPS, it became one of the standard dyes in the cardiac field due to its sub-millisecond response time, high sensitivity, long-term stability and comparably low phototoxicity [73–75].¹¹ This dye is used for all measurements in Sect. 3.3 which will be described in the following.¹²

2.3.1 Setup and Tissue Preparation

Most of the recordings presented in Sect. 3.3 are obtained on isolated atrial or ventricular preparations of adult beagle dogs. The experimental procedures for these animals were approved by the Institutional Animal Care and Use Committee of the Center for Animal Resources and Education at Cornell University. The procedure for tissue preparation is described in detail in the methods sections of Ref. [81] and [82]. Briefly, after excising the heart from anesthetized adult beagle dogs, physiological conditions are maintained by perfusing the tissue with 37 °C tyrode solution through the cannulated coronary arteries. The perfusion is also used to administer all drugs including di-4-ANEPPS. Atria or ventricles were cut open and flattened out in a bath, such that both epicardial and endocardial surfaces could be imaged. The setup for optically imaging cardiac electrical activity (excluding the perfusion) is depicted in Fig. 2.10: Di-4-ANEPPS in the sample is excited using LEDs (Luxeon LXHL-LM5C Green) with approximately 530 nm peak wave length. The emitted light is longpass filtered before it is detected by a high-resolution, high-speed camera, either a Photometrics Cascade 128+ or a Vision Research Phantom V7.

¹⁰ See Sect. 1.2.

¹¹ To optimize measurements for certain experimental requirements—e.g., simultaneous imaging of calcium and voltage or recording of optical signals from below the surface of the tissue—there is a search for alternatives, particularly in the long wave length range [76, 77].

¹² For further information on optical imaging in general, see Ref. [78–80].

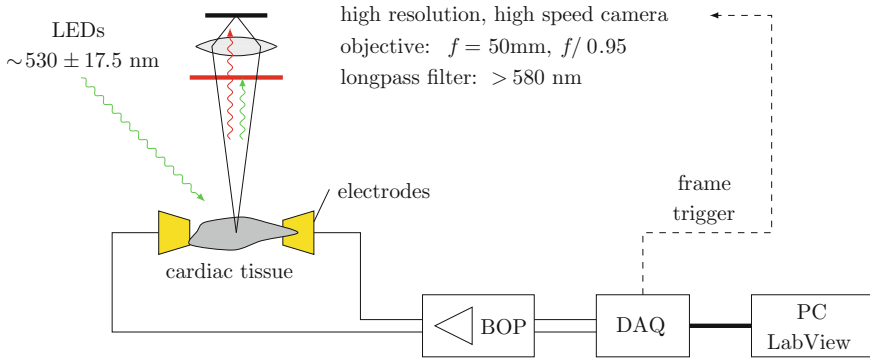


Fig. 2.10 Optical mapping setup. LEDs shine excitation light at the sample without additional excitation filters. The perfused cardiac tissue is loaded with voltage-sensitive dye (di-4-ANEPPS), whose excitation and emission spectra depend on the membrane potential. An emission filter is used to convert the specific spectral changes into an intensity change (cf. Fig. 2.11) that can be recorded with high-speed, high-resolution cameras equipped with EMCCD/CMOS sensors. The voltage between the electrodes is delivered by a power amplifier (Kepco BOP 100-4M), which is controlled by a custom written LabView program through a digital/analog data acquisition device (National Instruments DAQ USB-6259 BNC). Through the same device, the LabView program can trigger the acquisition of individual camera frames

The former acquires images of a maximum of 128×128 pixels at a maximum frame rate of about 500 Hz, which can be streamed to the hard disk of a PC in real time. This resolution is sufficient to resolve the spatio-temporal dynamics on the tissue surface during normal or arrhythmic activity and to accurately observe the activity induced by electric-field stimulation of quiescent tissue with low field strengths up to approximately 1.5 V/cm (see Sects. 2.3.3 and 2.3.4 for details). Due to limited buffer size, only short recordings of 600×800 pixels at 2 kHz were acquired with the Phantom camera for validation purposes and to verify that, for electric-field stimulation at higher field strengths when the dynamics is faster, the limited time resolution of the Cascade camera starts to impact the results. Due to nonuniform illumination and staining, the absolute intensity of light detected from different tissue regions varies greatly, which results in *motion artifacts*, when the tissue is moving. To ensure that there is a nearly constant relation between tissue locations and image pixels in the course of an excitation, Blebbistatin is used to suppress contraction of the tissue [83].

2.3.2 Optical Imaging

Under these conditions, the intensity change in the recorded images is a measure for the membrane voltage at the corresponding location. The spectral properties of the dye and of the hardware components used in the experiments described here

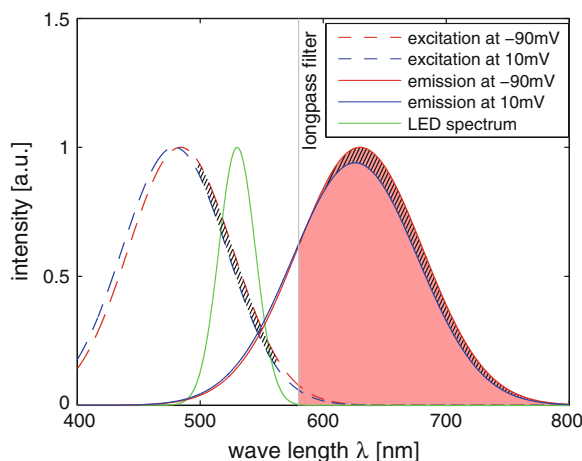


Fig. 2.11 Voltage-dependent excitation and emission spectra of di-4-ANEPPS. Excitation (*dashed lines*) and emission spectra (*full lines*) spectra are plotted for the resting membrane potential (*red*) and the depolarized state of the cell (*blue*). The *red area* under the *red curve* indicates the total intensity detected for the resting potential through a low pass emission filter. The area between the excitation curves is hatched where the LED intensity (*green*) is above 10 % of its peak value. The hatched area between the emission curves is the intensity change picked up by the camera due to the spectral shift and amplitude change

are illustrated in Fig. 2.11.¹³ The sample is illuminated using the above-mentioned LEDs without an excitation filter, which is possible due to the relatively narrow-banded light of 35 nm spectral half-width (green line). The LED spectrum overlaps almost exclusively with the long-wave-length edge of the excitation spectrum of the dye, which shifts a few nanometers to the left when the membrane is depolarized. As the excitation spectrum amplitude in the overlap region is lower during depolarization than at the resting potential, this results in a weaker excitation (hatched area between the dashed curves) of the dye and therefore an overall decrease in the emission amplitude, from the (full) red to the blue curve. Additionally, the emission spectrum is also voltage-sensitive and is shifted to the left. Due to the *Stokes shift*—the separation between the excitation and the emission spectrum—most of the excitation light can be kept away from the camera using a 580 nm longpass filter, such that, at resting potential, the camera detects the integrated intensity indicated by the red area. Due to the combined spectral shift and amplitude decrease, the intensity is reduced during depolarization by the hatched area between the full curves. The optical signal is therefore expected to yield *inverted action potentials*. The fractional intensity change is typically between 1 and 5 %.

¹³ Optical properties of di-4-ANEPPS were mainly extracted from a recent publication on ratiometric optical mapping [84], which contains collected and combined figures from a number of earlier studies (see also references therein). The properties of the LEDs can be found on the data sheet available at the manufacturer's website <http://www.luxeonstar.com/v/vspfiles/downloadables/DS30.pdf> (note, however, that the product line has been discontinued).

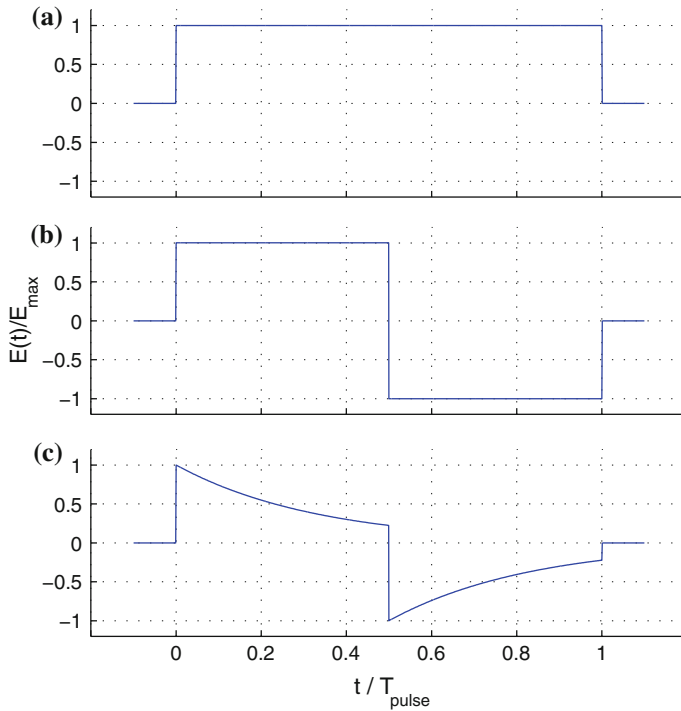


Fig. 2.12 Pulse shapes. Different pulse shapes used for stimulating the tissue. All waveforms are relative to the peak amplitude E_{\max} and the total pulse duration T_{pulse} . **a** Monophasic pulse. **b** Biphasic pulse. **c** Truncated exponential biphasic pulse mimicking a capacitor discharge. This waveform has another parameter τ_{decr} denoting the damping time constant. For the first half of the pulse, $E(t) = E_{\max} \exp(-t/\tau_{\text{decr}})$

2.3.3 Electric-Field Stimulation Experiments

Electric-field pulses are delivered using a power amplifier (Kepco BOP 100-4M) controlled by a custom-made LabView program and two plate electrodes placed on opposing sides of the bath (see Fig. 2.10). The field strength in the bath is calibrated by measuring the voltage between two wire electrodes placed at a known distance. For all experiments presented here, except those in Sect. 3.3.6, monophasic electric-field pulses with a duration of $T_{\text{pulse}} = 5$ ms were used (see Fig. 2.12). The experiments were carried out by A. Squires, F. H. Fenton, S. Luther and the author of this thesis. The work for this thesis led to significant improvements in the LabView software, automating the data acquisition for electric-field stimulation at different field strengths and with the different pulse shapes shown in Fig. 2.12. The follow-up experiments presented in Sect. 3.3.6 use this new software and were carried out by M. Chebbok, D. Hornung and the author.

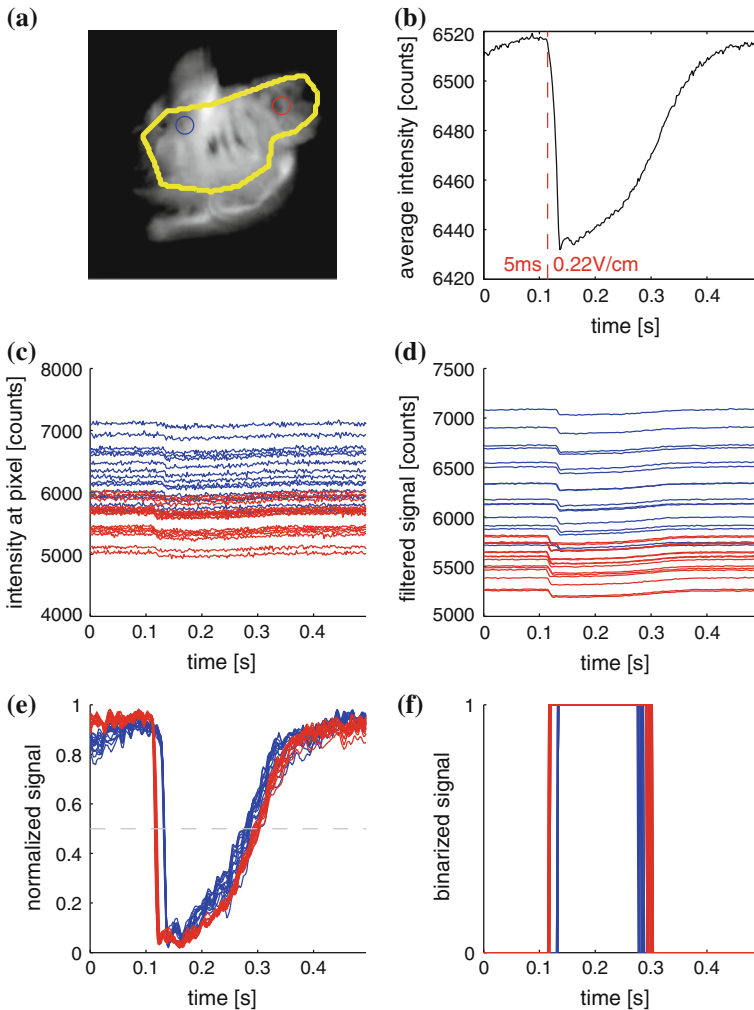


Fig. 2.13 Signal processing of optical mapping data. **a** Raw camera image showing the endocardial view of the sample. The *yellow line* indicates the mask of sufficient staining and fractional intensity change above noise level in the right atrium. **b** Average signal within the masked region after an electric field pulse of 5 ms duration at a field strength of 0.22 V/cm, indicated by *red dashed line*. **c** Raw signals at locations indicated by *colored circles* in **a**. **d** Spatially and temporally filtered signals at the same locations. **e** Signals normalized to maximum and minimum intensity. The *dashed gray line* indicates the threshold of binarization. **f** Binarized signal for activation detection

2.3.4 Signal Processing: Activation Maps

The raw images are acquired by the camera at a frequency of 0.5–2 kHz (depending on camera type and binning parameters) and then processed as depicted in Fig. 2.13. The area enclosed by the yellow line in the raw image of Fig. 2.13a was determined

retrospectively after carrying out the analysis. It contains a region that lies entirely within the tissue of one chamber (in this case: the right atrium) and has sufficient staining to provide a fractional intensity change (above noise level; approximately $>0.5\%$) which allows for reliable upstroke detection. In Fig. 2.13b, the averaged signal within the mask shows a single activation of the tissue which was evoked by an electric field pulse of 5 ms duration and field strength $E = 0.22$ V/cm. To reduce noise in the individual time traces for each pixel as plotted in Fig. 2.13c, a box filter is applied spatially (5×5 pixels) and temporally (3 frames). This results in time series for every pixel according to Fig. 2.13d. Each time series is then normalized by its individual minimum and maximum values to vary between 0 and 1, leading to the data as in Fig. 2.13e. From these time series, the activation of the tissue can be reliably detected using a simple threshold, usually 0.5. For the examples plotted in Fig. 2.13f, one can see that the tissue is activated earlier at the red location marked in Fig. 2.13a than at the blue one.

Assuming that the tissue is activated everywhere only once within a certain time window, an *activation map* can be constructed from the processed data:

$$T_a(x, y) := \min\{t \mid \hat{I}(x, y, t) < 0.5\} \quad \forall x, y \text{ within mask} \quad (2.102)$$

\hat{I} is the preprocessed and normalized intensity as shown in Fig. 2.13e, which depends on the spatial coordinates x, y and time t . For each camera pixel, T_a displays the time of activation, reducing the activation information contained in the time-varying signals to one static image. To reduce the probability of misdetections due to noise, an activation time is only accepted as such if the average value of the next 10 frames is also subthreshold. One common application of activation maps is the characterization of conduction velocities for arbitrary wave patterns [85–88]. An example map for the same data as in Fig. 2.13 is shown in Fig. 2.14. The earlier activation of the tissue at the location circled in red compared to the region circled in blue can be read off directly from the map (compare Fig. 2.13e, f).

When interpreting activation maps, one has to bear in mind that activity is only observed on the surface of the tissue. Wave fronts on the surface correspond to iso- T_a lines, but the conduction velocities estimated from the advancing wave fronts on the surface can at best be considered an *apparent velocity*, since the angle of inclination of the wave front with the surface is not known. Likewise, minima in an activation map correspond to points from which waves spread outwards. These are marked by crosses in Fig. 2.14a. Such locations can be considered *apparent wave sources*, but in general correspond to the break-through sites, where waves from different real wave source in the bulk of tissue appear first on the surface. Assuming an approximately constant conduction velocity within the tissue, it is reasonable to suspect that each of the apparent wave sources corresponds to at least one real wave source and the activation time of each apparent wave source is correlated with the distance of a real wave source from the surface [89]. Additionally, there could be an intrinsic *latency* of the onset of a propagating wave for near-threshold stimulation. In Fig. 2.14a, the two apparent wave sources on the left appear more than 10 ms later than the one on the right.

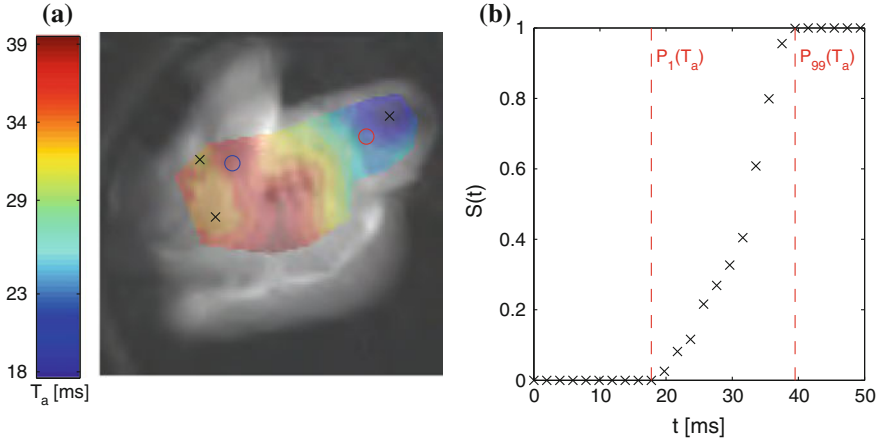


Fig. 2.14 Activation map. **a** Activation map T_a superimposed on a raw image of the atrial tissue preparation. Circles indicate the locations considered in Fig. 2.13, crosses mark minima

The activation time τ is defined as

$$\tau = P_{99}(T_a) - P_1(T_a), \quad (2.103)$$

where $P_n(T_a)$ is the n th percentile of activation times within the masked region. In Sect. 3.3, τ will be used to quantify the number of sources created in the tissue as a response to the electric field. Essentially, this is the time from the observation of the first wave on the surface to the time of full activation of the considered tissue domain. Taking the percentiles instead of the actual minimum and maximum values is a precaution to remove outliers stemming from misdetected activation times. In a graph of the fractional area $S(t)$ activated until a given time t (with respect to the mask), these percentiles can be visualized as depicted in Fig. 2.14b.

It should be noted that, a priori, the definition of τ is *not* equivalent to the time from the stimulation to full activation of the tissue, as the first activation at time $\min_{x,y}(T_a(x, y))$ can occur some time after the pulse. In order to obtain sufficient statistics, recordings from a large number of experiments carried out over a time of several years (even before the beginning of the work for this thesis) had to be screened in terms of optical signal quality and stability of the preparation. For many of those measurements, camera recordings and electric-field stimulation were initiated independently of each other, rendering a determination of the stimulation time relative to the recorded frames impossible. Instead, the definition of Eq. (2.103) will be used, which is independent of the actual time of the pulse. There are, however, two reasons why this definition is not expected to alter the results significantly: Firstly, as will be seen in the development of the theoretical tools in Sect. 3.3, the approximations derived there are only valid for a large number of wave sources distributed approximately homogeneously throughout the tissue. If this is the case, then there

will certainly be a wave source near the surface of the tissue, calibrating $P_1(T_a)$ to the time of the pulse. Secondly, the same theory will assume that waves propagate with a constant velocity from the wave sources, starting instantaneously at a given time. However, in reality, there may be a certain latency in the response of the tissue, especially for lower field strengths. Furthermore, the pulse has a finite duration, so the starting time of wave propagation is not well defined even without latency, and using either the beginning or the end of pulse as a reference time is inaccurate, too. From this viewpoint, assuming that the waves begin to propagate when the first activation on the surface is observed might even be a more realistic approximation. For consistency, the activation time τ as defined in Eq. (2.103) is used for all results presented in Sect. 3.3.

References

1. Hodgkin, A. L., & Huxley, A. F. (1952). A quantitative description of membrane current and its application to conduction and excitation in nerve. *Journal of Physiology*, 117, 500–544.
2. Hodgkin, A. L., Huxley, A. F., & Katz, B. (1952). Measurement of current-voltage relations in the membrane of the giant axon of Loligo. *Journal of Physiology*, 116, 424–448.
3. Hodgkin, A. L., & Huxley, A. F. (1952). The dual effect of membrane potential on sodium conductance in the giant axon of Loligo. *Journal of Physiology*, 116, 497–506.
4. Hodgkin, A. L., & Huxley, A. F. (1952). Currents carried by sodium and potassium ions through the membrane of the giant axon of Loligo. *Journal of Physiology*, 116, 449–472.
5. Hodgkin, A. L., & Huxley, A. F. (1952). The components of membrane conductance in the giant axon of Loligo. *Journal of Physiology*, 116, 473–496.
6. Cole, K. (1949). Dynamic electrical characteristics of the squid axon membrane. *Archives des Sciences Physiologiques*, 3, 253–258.
7. Marmont, G. (1949). Studies on the axon membrane: I. A new method. *Journal of Cellular Physiology*, 34, 351–382.
8. Noble, D. (1962). A modification of the Hodgkin-Huxley equations applicable to Purkinje fibre action and pace-maker potentials. *Journal of Physiology*, 160, 317–352.
9. Noble, D. (1966). Applications of Hodgkin-Huxley equations to excitable tissues. *Physiological Reviews*, 46, 1–50.
10. Zhao, Y., et al. (2009). Patch clamp technique: Review of the current state of the art and potential contributions from nanoengineering. *Proceedings of the Institution of Mechanical Engineers, Part N: Journal of Nanoengineering and Nanosystems*, 222, 1–11.
11. Tammaro, P., Shimomura, K., & Proks, P. (2008). Xenopus oocytes as a heterologous expression system for studying ion channels with the patch-clamp technique. *Methods in Molecular Biology (Clifton, NJ)*, 491, 127–139.
12. Heimburg, T., & Jackson, A. D. (2005). On soliton propagation in biomembranes and nerves. *Proceedings of the National Academy of Sciences of the United States of America*, 102, 9790–9795.
13. Heimburg, T., & Jackson, A. D. (2007). On the action potential as a propagating density pulse and the role of anesthetics. *Biophysical Reviews and Letters*, 02, 57–78.
14. Heimburg, T. (2012). The capacitance and electromechanical coupling of lipid membranes close to transitions: The effect of electrostriction. *Biophysical Journal*, 103, 918–929.
15. Wang, L. J., & Sobie, E. A. (2008). Mathematical model of the neonatal mouse ventricular action potential. *American Journal of Physiology: Heart and Circulatory Physiology*, 294, H2565–H2575.

16. Grant, A. O. (2009). Cardiac ion channels. *Circulation: Arrhythmia and Electrophysiology*, 2, 185–194.
17. Fox, R. F. (1997). Stochastic versions of the Hodgkin-Huxley equations. *Biophysical Journal*, 72, 2068–2074.
18. Goldwyn, J. H., Imennov, N. S., Famulare, M., & Shea-Brown, E. (2011). Stochastic differential equation models for ion channel noise in Hodgkin-Huxley neurons. *Physical Review E*, 83, 041908.
19. Clark, J., & Plonsey, R. (1966). A mathematical evaluation of the core conductor model. *Biophysical Journal*, 6, 95–112.
20. Spach, M. S., & Barr, R. C. (1976). Origin of epicardial ST-T wave potentials in the intact dog. *Circulation Research*, 39, 475–487.
21. Miller, W. T., & Geselowitz, D. B. (1978). Simulation studies of the electrocardiogram. I. The normal heart. *Circulation Research*, 43, 301–315.
22. Spach, M. S., Miller, W. T., Miller-Jones, E., Warren, R. B., & Barr, R. C. (1979). Extracellular potentials related to intracellular action potentials during impulse conduction in anisotropic canine cardiac muscle. *Circulation Research*, 45, 188–204.
23. Roth, B., & Wikswo, J. (1986). A bidomain model for the extracellular potential and magnetic field of cardiac tissue. *IEEE Transactions on Biomedical Engineering*, 33, 467–469.
24. Roth, B. (1991). Action potential propagation in a thick strand of cardiac muscle. *Circulation Research*, 68, 162–173.
25. Clayton, R. H., et al. (2011). Models of cardiac tissue electrophysiology: Progress, challenges and open questions. *Progress in Biophysics and Molecular Biology*, 104, 22–48.
26. Fenton, F. H., Cherry, E. M., Karma, A., & Rappel, W. (2005). Modeling wave propagation in realistic heart geometries using the phase-field method. *Chaos*, 15, 013502.
27. Bueno-Orovio, A., Pérez-García, V. M., & Fenton, F. H. (2006). Spectral methods for partial differential equations in irregular domains: The spectral smoothed boundary method. *SIAM Journal on Scientific Computing*, 28, 886–900.
28. Bueno-Orovio, A., Cherry, E. M., & Fenton, F. H. (2008). Minimal model for human ventricular action potentials in tissue. *Journal of Theoretical Biology*, 253, 544–60.
29. Li, X., Lowengrub, J., Rätz, A., & Voigt, A. (2009). Solving PDEs in complex geometries: A diffuse domain approach. *Communications in Mathematical Sciences*, 7, 81–107.
30. Baudoin, F. (2012). *Diffusion semi-group lectures*, (Wordpress.com). Lecture 3: The heat equation associated to a diffusion operator. <http://fabricebaudoin.wordpress.com/2012/03/28/lecture-3-the-heat-equation-associated-to-a-diffusion-operator/>.
31. Fenton, F. H. & Cherry, E. M. (2008). Models of cardiac cell. *Scholarpedia*, 3, 1868. http://www.scholarpedia.org/article/Models_of_cardiac_cell.
32. Barkley, D., Kness, M., & Tuckerman, L. (1990). Spiral-wave dynamics in a simple model of excitable media: The transition from simple to compound rotation. *Physical Review A*, 42, 2489–2492.
33. Fenton, F. H., & Karma, A. (1998). Vortex dynamics in three-dimensional continuous myocardium with fiber rotation: Filament instability and fibrillation. *Chaos*, 8, 20–47.
34. Barkley, D. (1991). A model for fast computer simulation of waves in excitable media. *Physica D*, 49, 61–70.
35. FitzHugh, R. (1961). Impulses and physiological states in theoretical models of nerve membrane. *Biophysical Journal*, 1, 445–466.
36. Nagumo, J., Arimoto, S., & Yoshizawa, S. (1962). An active pulse transmission line simulating nerve axon. *Proceedings of the IRE*, 50, 2061–2070.
37. Bä, M., & Eiswirth, M. (1993). Turbulence due to spiral breakup in a continuous excitable medium. *Physical Review E*, 48, R1635–R1637.
38. Fenton, F. H., Cherry, E. M., Hastings, H., & Evans, S. (2002). Multiple mechanisms of spiral wave breakup in a model of cardiac electrical activity. *Chaos*, 12, 852–892.
39. Gray, R., Pertsov, A., & Jalife, J. (1998). Spatial and temporal organization during cardiac fibrillation. *Nature*, 392, 75–78.

40. Witkowski, F., et al. (1998). Spatiotemporal evolution of ventricular fibrillation. *Nature*, 392, 78–82.
41. Iyer, A., & Gray, R. (2001). An experimentalist's approach to accurate localization of phase singularities during reentry. *Annals of Biomedical Engineering*, 29, 47–59.
42. Bray, M., Lin, S.-F., Aliev, R., Roth, B., & Wikswo, J. (2001). Experimental and theoretical analysis of phase singularity dynamics in cardiac tissue. *Journal of Cardiovascular Electrophysiology*, 12, 716–722.
43. Clayton, R., Zhuchkova, E., & Panfilov, A. (2006). Phase singularities and filaments: Simplifying complexity in computational models of ventricular fibrillation. *Progress in Biophysics and Molecular Biology*, 90, 378–398.
44. Mermin, N. (1979). Topological theory of defects in ordered media. *Reviews of Modern Physics*, 51, 591–648.
45. Oseledec, V. I. A. (1968). multiplicative ergodic theorem. Ljapunov characteristic numbers for dynamical systems. *Transaction of the Moscow Mathematical Society*, 19, 197–231.
46. Ruelle, D. (1979). Analytic properties of the characteristic exponents of random matrix products. *Advances in Mathematics*, 32, 68–80.
47. Ruelle, D. (1979). Ergodic theory of differentiable dynamical systems. *Publications Mathématiques de l'IHÉS*, 50, 27–58.
48. Raghunathan, M. S. (1979). A proof of Oseledec's multiplicative ergodic theorem. *Israel Journal of Mathematics*, 32, 356–362.
49. Benettin, G., Galgani, L., Giorgilli, A., & Strelcyn, J.-M. (1980). Lyapunov characteristic exponents for smooth dynamical systems and for hamiltonian systems; a method for computing all of them. Part 1: Theory. *Meccanica*, 15, 9–20.
50. Benettin, G., Galgani, L., Giorgilli, A., & Strelcyn, J.-M. (1980). Lyapunov characteristic exponents for smooth dynamical systems and for hamiltonian systems; a method for computing all of them. Part 2: Numerical application. *Meccanica*, 15, 21–30.
51. Eckmann, J., & Ruelle, D. (1985). Ergodic theory of chaos and strange attractors. *Reviews of Modern Physics*, 57, 617–656.
52. Kuptsov, P. V., & Parlitz, U. (2012). Theory and computation of covariant Lyapunov vectors. *Journal of Nonlinear Science*, 22, 727–762.
53. Ginelli, F., et al. (2007). Characterizing dynamics with covariant Lyapunov vectors. *Physical Review Letters*, 99, 130601.
54. Wolfe, C. L., & Samelson, R. M. (2007). An efficient method for recovering Lyapunov vectors from singular vectors. *Tellus Series A: Dynamic Meteorology and Oceanography*, 59, 355–366.
55. Szendro, I. G., Pazo, D., Rodriguez, M. A., & Lopez, J. M. (2007). Spatiotemporal structure of Lyapunov vectors in chaotic coupled-map lattices. *Physical Review E*, 76, 025202.
56. Pazo, D., Szendro, I. G., Lopez, J. M., & Rodriguez, M. A. (2008). Structure of characteristic Lyapunov vectors in spatiotemporal chaos. *Physical Review E*, 78, 016209.
57. Yang, H., Takeuchi, K. A., Ginelli, F., Chate, H., & Radons, G. (2009). Hyperbolicity and the effective dimension of spatially extended dissipative systems. *Physical Review Letters*, 102, 074102.
58. Hoover, W., & Hoover, C. G. (2012). Local Gram-Schmidt and covariant Lyapunov vectors and exponents for three harmonic oscillator problems. *Communications in Nonlinear Science and Numerical Simulation*, 17, 1043–1054.
59. Strikwerda, J. (2004). *Finite difference schemes and partial differential equations* (2nd ed.). Philadelphia, PA, USA: Society for Industrial and Applied Mathematics (SIAM). http://books.google.de/books?id=SH8R_fIzBGIC.
60. Press, W. H., Teukolsky, S. A., Vetterling, W. T. & Flannery, B. P. *Numerical recipes in C: The art of scientific computing* (2nd ed.). New York, NY, USA: Cambridge University Press.
61. Cherry, E. M., Greenside, H. S., & Henriquez, C. S. (2003). Efficient simulation of three-dimensional anisotropic cardiac tissue using an adaptive mesh refinement method. *Chaos*, 13, 853–865.
62. Hornung, D. (2013). *Cardiac arrhythmia termination on the vascular and organ scale*. Ph.D. Thesis, University of Göttingen.

63. Behrend, A. (2011). *Interaction of pinned spiral waves with a pulsed electric field in heterogeneous excitable media*. Diploma Thesis, University of Göttingen.
64. Linke, P. (2012). *Segmentation of a human whole heart scan and simulation of the cardiac electrical conduction system*. Bachelor's Thesis, University of Göttingen.
65. Mayer, A. (2012). *Spatio-temporal dynamics in a numerical model for ventricular tissue of neonatal mice*. Bachelor's Thesis, University of Göttingen.
66. Tom Wörden, H. (2012). *Simulation of the electrical activity of heart tissue using the bidomain model*. Bachelor's Thesis, University of Göttingen.
67. MATLAB Natick, Massachusetts, USA: The MathWorks Inc. <http://www.mathworks.com/>.
68. Cohen, L. B., Keynes, R. D., & Hille, B. (1968). Light scattering and birefringence changes during nerve activity. *Nature*, 218, 438–441.
69. Tasaki, I., Watanabe, A., Sandlin, R., & Carnay, L. (1968). Changes in fluorescence, turbidity, and birefringence associated with nerve excitation. *Proceedings of the National Academy of Sciences of the United States of America*, 61, 883–888.
70. Salzberg, B. M., Davila, H. V., & Cohen, L. B. (1973). Optical recording of impulses in individual neurones of an invertebrate central nervous system. *Nature*, 246, 508–509.
71. Salama, G., & Morad, M. (1976). Merocyanine 540 as an optical probe of transmembrane electrical activity in the heart. *Science*, 191, 485–487.
72. Salama, G. (1979). Optical probes of membrane potential in heart muscle. *Journal of Physiology*, 292, 267–295.
73. Loew, L. M. (1982). Design and characterization of electrochromic membrane probes. *Journal of Biochemical and Biophysical Methods*, 6, 243–260.
74. Fluhler, E., Burnham, V. G., & Loew, L. M. (1985). Spectra, membrane binding, and potentiometric responses of new charge shift probes. *Biochemistry*, 24, 5749–5755.
75. Montana, V. (1992). A naphthyl analog of the aminostyryl pyridinium class of potentiometric membrane dyes shows consistent sensitivity in a variety of tissue, cell, and model membrane preparations. *Journal of Membrane Biology*, 130, 1–10.
76. Salama, G., et al. (2005). Properties of new, long-wavelength, voltage-sensitive dyes in the heart. *Journal of Membrane Biology*, 208, 125–140.
77. Matiukas, A. (2006). New near-infrared optical probes of cardiac electrical activity. *American Journal of Physiology: Heart and Circulatory Physiology*, 290, H2633–H2643.
78. Efimov, I. R. (2004). Optical imaging of the heart. *Circulation Research*, 95, 21–33.
79. Efimov, I., & Salama, G. (2012). The future of optical mapping is bright: RE: Review on: "Optical imaging of voltage and calcium in cardiac cells and tissues" by Herron, Lee, and Jalife. *Circulation Research*, 110, e70–e71.
80. Herron, T. J., Lee, P., & Jalife, J. (2012). Optical imaging of voltage and calcium in cardiac cells & tissues. *Circulation Research*, 110, 609–623.
81. Luther, S., et al. (2011). Low-energy control of electrical turbulence in the heart. *Nature*, 475, 235–239.
82. Fenton, F. H., et al. (2009). Termination of atrial fibrillation using pulsed low-energy far-field stimulation. *Circulation*, 120, 467–474.
83. Fedorov, V. V., et al. (2007). Application of blebbistatin as an excitation-contraction uncoupler for electrophysiologic study of rat and rabbit hearts. *Heart Rhythm*, 4, 619–626.
84. Bachtel, A. D., et al. (2011). A novel approach to dual excitation ratiometric optical mapping of cardiac action potentials with di-4-ANEPPS using pulsed led excitation. *IEEE Transactions on Biomedical Engineering*, 58, 2120–2126.
85. Morley, G., et al. (1999). Characterization of conduction in the ventricles of normal and heterozygous cx43 knockout mice using optical mapping. *Journal of Cardiovascular Electrophysiology*, 10, 1361–1375.
86. Nygren, A., et al. (2000). Voltage-sensitive dye mapping of activation and conduction in adult mouse hearts. *Annals of Biomedical Engineering*, 28, 958–967.
87. Mourad, A., & Nash, M. P. (2007). Method for quantifying conduction velocity during ventricular fibrillation. *Physical Review E*, 75, 011914.

88. Petitprez, S., et al. (2010). SAP97 and dystrophin macromolecular complexes determine two pools of cardiac sodium channels Nav1.5 in cardiomyocytes. *Circulation Research*, 108, 294–304.
89. Zemlin, C., Mironov, S., & Pertsov, A. (2006). Near-threshold field stimulation: Intramural versus surface activation. *Cardiovascular Research*, 69, 98–106.

Complex Structure and Dynamics of the Heart

Bittihn, P.

2015, XV, 204 p. 69 illus., 47 illus. in color., Hardcover

ISBN: 978-3-319-12231-1